Sensitivity of cirrus and contrail radiative effect on cloud microphysical and environmental parameters.

Kevin Wolf[1], Nicolas Bellouin[1,2], and Olivier Boucher[1]

[1]Institut Pierre-Simon Laplace, Sorbonne Université / CNRS, Paris, France
[2]Department of Meteorology, University of Reading, Reading, United Kingdom

Correspondence: Kevin Wolf (kevin.wolf@ipsl.fr)

Abstract. Natural cirrus clouds and contrails cover about 30% of the Earth's mid-latitudes and up to 70% of the Tropics. Due to their widespread occurrence, cirrus have a considerable impact on the Earth energy budget, which, on average, leads to a warming net radiative effect (solar + thermal-infrared). However, whether the instantaneous radiative effect (RE), which in some cases corresponds to a radiative forcing, of natural cirrus or contrails is positive or negative depends on their microphys-
ical, macrophysical, and optical properties, as well as the radiative properties of the environment. This is further complicated by the fact that the actual ice crystal shape is often unknown and, thus, ice clouds remain one of the components that are least understood in the Earth's radiative budget.

The present study aims to investigate the dependency of the effect on cirrus RE on eight parameters: solar zenith angle, ice water content, ice crystal effective radius, cirrus temperature, surface albedo, surface temperature, cloud optical thickness of an
underlying liquid water cloud, and three ice crystal shapes. In total, 283,500 plane-parallel radiative transfer simulations have been performed, not including three-dimensional scattering effects. Parameter ranges are selected that are typically associated with natural cirrus and contrails. In addition, the effect of variations in the relative humidity profile and the ice cloud geometric thickness have been investigated for a sub-set of the simulations. The multi-dimensionality and complexity of the 8-dimensional parameter space makes it impractical to discuss all potential configurations in detail. Therefore, specific cases are selected and
discussed.

For a given parameter combination, the largest impact on solar, thermal-infrared (TIR), and net RE is related to the ice crystal effective radius. The second most important parameter is ice water content, which equally impacts the solar and terrestrial RE. Solar RE of cirrus is also determined by solar zenith angle, surface albedo, liquid cloud optical thickness, and ice crystal shape in descending priority. RE in the TIR spectrum is dominated by surface temperature, ice cloud temperature, liquid water cloud
optical thickness, and ice crystal shape. Net RE is controlled by surface albedo, solar zenith angle, and surface temperature in decreasing importance. The relative importance of the studied parameters differs depending on the ambient conditions. Furthermore, and during nighttime the net RE is equal to the TIR RE.

The data set generated in this work is publicly available. It can be used as a look-up-table to extract the RE of cirrus clouds, contrails, and contrail cirrus instead of full radiative transfer calculations.

1 Introduction

Cirrus clouds cover large areas of the Earth, with cloud cover estimates of 30 % in the mid-latitudes and up to 70 % in the tropics (Liou, 1986; Wylie and Menzel, 1999; Chen et al., 2000; Sassen et al., 2008; Nazaryan et al., 2008). Due to their widespread occurrence, cirrus can have a considerable impact on the global energy budget. In addition to cirrus, air traffic leads to the formation of condensation trails, also termed contrails, which are geometrically and optically thin clouds with similar radiative effects as thin natural cirrus (Liou, 1986). For the sake of simplicity, the term cirrus is used interchangeably for natural cirrus, contrail-induced cirrus, and contrails throughout this article.

Depending on ambient conditions, contrails are short lived (t < 10 min) but can persist up to a day, when the surrounding air mass is sufficiently cold and moist (Schumann, 1996; Haywood et al., 2009; Schumann and Heymsfield, 2017; Kärcher, 2018). In such conditions, persistent contrails transition from line-shaped clouds to larger cloud fields (Unterstrasser and Stephan, 2020). Modeling and satellite studies have estimated that contrail and contrail-induced cirrus cloud cover can reach up to 6 to 10 % over Europe (Burkhardt and Kärcher, 2011; Quaas et al., 2021) and significantly contribute to high-level cloudiness over Europe (Schumann et al., 2015, 2021).

Under most circumstances cirrus have a cooling effect in the solar wavelength range (0.2–3.5 μm, sometimes called short-wave) and a heating effect in the thermal-infrared (TIR) wavelength range (3.5–75 μm, sometimes also termed longwave or terrestrial). The net radiative effect (solar cooling + TIR warming) is often a warming as the TIR effect dominates (Chen et al., 2000). By combining satellite observations and radiative transfer (RT) simulations, Chen et al. (2000) estimated a global annual mean cirrus cloud radiative effect (RE) of -25.3 W m^{-2} in the solar wavelength range and 30.7 W m^{-2} in the TIR wavelength range, leading to a positive net effect of 5.4 W m^{-2}. However, whether the instantaneous RE of natural cirrus or contrails is positive or negative depends on their microphysical, macrophysical, and optical, as well as radiative properties of the environment. The cloud properties relevant to the RE of the cloud are primarily cloud altitude, cloud temperature, ice water content, ice crystal shape (also called crystal habit), and the orientation of the ice crystals (Fu and Liou, 1993; Stephens et al., 2004; Campbell et al., 2016). Furthermore, the underlying surface properties, i.e., surface albedo and surface temperature, as well as gaseous absorption and additional underlying cloud layers, also have an effect on the cirrus RE. Dynamical processes in the atmosphere have a strong influence on those parameters, for example lifting of air masses along warm conveyor belts or cloud anvils, that lead to a variety of ice crystal shapes and crystal surface roughness (Freudenthaler et al., 1996; Wendisch et al., 2007; Yang et al., 2010; Krämer et al., 2016; Luebke et al., 2016). As a result, the actual distribution of crystal shapes within a cirrus and the related RE are often unclear. Thus ice clouds remain one of the components that is least understood in the Earth's radiative budget (Stevens and Bony, 2013; Bauer et al., 2015; Bickel et al., 2020) and this lack of understanding contributes to uncertainties in the climate impact of aviation (Lee et al., 2021).

To estimate the radiative impact of a cloud as well as related potential uncertainties and sensitivities, RT simulations represent a helpful tool. While the atmospheric RT in liquid water clouds composed of spherical cloud droplets can rely on geometric optics or Mie-scattering theory (Mie, 1908; van de Hulst, 1981), RT in ice clouds is complicated by the non-spherical crystal shape and the interaction with incoming radiation, i.e., through their single-scattering phase function. The single-scattering

phase function, for example, has to be determined by computationally-expensive methods, like ray tracing (Bi et al., 2014),

60 Monte Carlo simulations (Macke et al., 1996a, b), or the T-matrix method (Mishchenko, 2020). Due to the computational burden of such accurate simulations, parameterizations of ice crystal properties are often developed and validated against the more precise calculations (Takano and Liou, 1989; Fu, 1996; Yang et al., 2000, 2013). More recent ice crystal parameterizations by Yang et al. (2000), Baum et al. (2005a, b), Baum et al. (2007), and Yang et al. (2013) in combination with the latest RT models allow to determine the radiative impact of cirrus clouds with acceptable computational cost and accuracy. By varying

65 the microphysical and macrophysical properties of the cirrus, as well as the surface properties in the RT model, the natural range of cirrus and their environment can be represented and the RE can be estimated. Furthermore, uncertainties due to the insufficiently known crystal shape can be assessed.

Multiple studies that aimed to investigate the impact of a certain parameter on cloud RE have been performed in the past. Fu and Liou (1993) as well as Yang et al. (2010) focused on the effects of the selected ice crystal habit and ice water path. The effect

70 of the ice crystal size distribution was analyzed, for example, by Zhang et al. (1999) or Mitchell et al. (2011). A comprehensive study of cirrus radiative effects was conducted by Schumann (2012), who aimed to derive a parameterization to estimate the cloud RE. While those studies are valuable, none of them investigate the effect of multiple factors, like relevant cloud and environmental input parameters. These studies have identified parameters that affect cirrus RE, but all these parameters need to be considered together, including both cloud and environmental parameters. This article is intended as a parametric sensitivity

75 study that aims to compare the effects of major parameters. Furthermore, we identify the driving parameters of RE by sampling the input parameter range, restricted to values that are typically associated with ice clouds. Finally, we provide an open-access data set, which allows the user to extract cloud REs for user-specific combinations of the input parameters. The look-up-table could in fact be coupled with models of any complexity, as long as they simulate the dimensions of the data set, namely: solar zenith angle, ice cloud temperature, surface albedo, ice water content, surface temperature, ice crystal effective radius, and

80 liquid water cloud optical thickness.

The study is structured in the following way. Section 2 introduces the selected parameter space, the RT model, and outlines basic definitions as well as methods used in the paper. Subsequently, Section 3 presents the results from the RT simulations. Because our simulations assume plane-parallel atmosphere and homogeneous clouds, Section 4 discusses 3-dimensional RT. That is followed by the summary in Sec. 5.

85 ## 2 Methods and Definitions

2.1 Definition of radiative effect and albedo

The radiative impact of a perturbation, e.g., clouds, is quantified by the concept of the radiative effect (RE). The RE is defined as the net difference in downward and upward irradiance ($F^\downarrow - F^\uparrow$) between the perturbed and unperturbed condition. In the case of clouds, the cloud radiative effect (CRE, denoted here as ΔF) is the difference in fluxes between the cloud (F_c) and

90   cloud-free (F_{cf}) atmosphere at a given altitude z (Ramanathan et al., 1989; Stapf et al., 2021; Luebke et al., 2022):

$$\Delta F(z) = F_c(z) - F_{cf}(z) = \left[F^\downarrow(z) - F^\uparrow(z) \right]_c$$
$$- \left[F^\downarrow(z) - F^\uparrow(z) \right]_{cf}, \tag{1}$$

where the upward and downward, cloudy and cloud-free irradiances are all counted positive. The net RE is given by:

$$\Delta F_{net}(z) = \Delta F_{sol}(z) + \Delta F_{TIR}(z), \tag{2}$$

which can be split into a solar and a thermal-infrared component. Within this study, the CRE is calculated for the top of
95   atmosphere (TOA), which is set in the radiative transfer calculations to an altitude of 120 km, unless stated otherwise.

In addition to the RE, the albedo α describes the interaction of a cloudy scene or a surface with the solar, incident radiation. The scene albedo $\alpha_{sol}(z = TOA)$ at the TOA is defined as the ratio of the reflected, upward irradiance $F^\uparrow_{sol}$ at TOA in relation to the incident, downward irradiance $F^\downarrow_{sol}$ at TOA and is given by:

$$\alpha_{sol,TOA} = \frac{F^\uparrow_{sol}(z = TOA)}{F^\downarrow_{sol}(z = TOA)}. \tag{3}$$

100   Similarly, the surface albedo $\alpha_{sol,srf}$ is calculated with $F^\uparrow_{sol,srf}$ and $F^\downarrow_{sol,srf}$ the respective irradiances at the surface ($z = 0$ km).

2.2   Radiative transfer simulation set-up

Upward and downward irradiances $F^\uparrow$ / $F^\downarrow$ were simulated with the library for Radiative transfer (libRadtran, Emde et al., 2016). The solar irradiances F_{sol} cover a wavelength range from 0.3 to 3.5 μm, which represents 97.7 % of the total incoming solar radiation (0–10 μm) calculated from the spectrum provided by Kurucz (1992). The thermal infrared (TIR) irradiances
105   include wavelengths from 3.5 to 75 μm, representing 99.3 % of the integrated blackbody radiation (3.5 to 100 μm) at 285 K (12°C).

The RT simulations are performed with the one–dimensional (1D) solver DISORT (Stamnes et al., 1988; Buras et al., 2011), which is part of libRadtran. Clouds are assumed to be horizontally uniform and lateral photon transport between columns is neglected, which is called the independent pixel approximation (IPA, Stephens et al., 1991; Cahalan et al., 1994). As the
110   main objective of this study is to map the basic dependencies of ΔF on the driving parameters, we neglect any variability in the spatial ice water content (IWC) distribution that exists in cirrus (Minnis et al., 1999). We also restrict the simulations to fully cloud covered scenes. The required number of streams was iteratively determined and set to 16 streams, which provides sufficient accuracy while limiting computational time. The trade-off between accuracy and computational time is detailed in Appendix C. The spectral TOA solar irradiance is provided by Kurucz (1992). The RT simulations consider molecular
115   absorption using the 'coarse' resolution REPTRAN parameterization from Gasteiger et al. (2014). Absorption by water vapor, carbon dioxide, ozone, nitrous oxide, carbon monoxide, methane, oxygen, and nitrogen and nitrogen dioxide is included in the simulations (Anderson et al., 1986; Emde et al., 2016).

The sensitivity of solar, TIR, and net cloud RE ΔF is estimated by varying eight parameters. The parameter ranges were chosen to represent commonly observed cirrus and contrail cirrus properties, as well as environmental parameters.

- The daily course of the Sun position is represented by solar zenith angles θ ranging from $0°$ and $85°$. Larger θ values are omitted to avoid numerical instability that would require more streams in the calculation. Furthermore, RT simulations with the DISORT solver for $\theta > 85°$ have to be interpreted with caution as DISORT does not consider the sphericity of the Earth and treats atmospheric layers as plane-parallel (Stamnes et al., 1988; Buras et al., 2011). In addition, differences between 1D and three–dimensional (3D) RT simulations increase significantly with values of up to $40\,\%$ (Gounou and Hogan, 2007; Forster et al., 2012).

- The Earth's surface albedo, α_{srf} ranges from 0 to 1, which represents the full possible range. In general, α_{srf} varies spectrally but here is kept constant for all solar wavelength. It is varied between 0 and 1 to include surface conditions ranging from open ocean to full sea ice or snow (Baldridge et al., 2009; Gardner and Sharp, 2010; Meerdink et al., 2019; Gueymard et al., 2019). Values of α_{srf} are given in Table 4. In the TIR wavelength range α_{srf} is assumed to be 0, which leads to an emissivity $\epsilon = 1$ with the Earth's surface thus acting as a blackbody (Wilber, 1999).

- Three atmospheric profiles (AP) are selected to represent subarctic, mid-latitude, and tropical conditions. The simulations are based on the subarctic winter (afglsw), the US standard (afglus), and the tropical (afglt) profiles after Anderson et al. (1986). Surface temperatures T_{srf} of $-15.95°C$ (subarctic winter), $14.85°C$ (US standard), and $26.55°C$ (tropical) are defined in libRadtran by the lower most temperature in the APs. The profile of relative humidity is linked to the AP via the Clausius–Clapeyron-equation (Corti and Peter, 2009). Variations in the water vapor (WV) profile primarily impact the RT in the TIR wavelength range, particularly in WV absorption bands, while RT in the solar wavelength range is less affected (Liou, 1992). The cirrus cloud top temperatures $T_{\mathrm{cld,ice}}$ are selected to span the temperature range in which contrails and cirrus typically form (Krämer et al., 2020). Here we cover a range from 219 to 243 K. The resulting ice cloud top altitudes $z_{\mathrm{ice,CT}}$ are set to the altitude, where the temperature in the APs equals the desired $T_{\mathrm{cld,ice}}$. $z_{\mathrm{ice,CT}}$ is found by linear interpolation between the altitude and temperature levels. Cirrus temperatures and related $z_{\mathrm{ice,CT}}$ are listed in Table 1. Within the simulations, the ice cloud geometric thickness dz is set to 1000 m for all simulations, which represents an average for observed contrails as well as natural cirrus (Freudenthaler et al., 1995; Sassen and Campbell, 2001; Noël and Haeffelin, 2007; Iwabuchi et al., 2012).

- Three different ice crystal shapes, namely: i) '8–column–aggregates' (called 'aggregates' thereafter), agglomerations of 8–columnar ice crystals; ii) 'droxtals', almost spherical ice crystals; and iii) 'plates' are used. These three shapes are selected to represent different stages in the temporal evolution of contrails. Several airborne in situ measurement campaigns that targeted cirrus and contrails imply that aggregates are the dominating ice crystal habit (Liu et al., 2014; Holz et al., 2016; Järvinen et al., 2018). For example, Järvinen et al. (2018) found that 61 to $81\,\%$ of the sampled ice crystals were aggregates with a rough surface. Such ice crystals are also assumed in current remote sensing applications of ice cloud, e.g., in the re-defined ice optical properties used by the Moderate Resolution Imaging Spectroradiometer (MODIS) Collection 6 product (Yang et al., 2013; Holz et al., 2016; Platnick et al., 2017; Forster and Mayer, 2022). Therefore, we selected 8–column–aggregates as the primary ice crystal habit. The second most observed habit are plate-like ice crystals (Holz et al., 2016; Forster et al., 2017; Järvinen et al., 2018), which are included in the simulations as a

Table 1. Surface temperature, cloud top temperature, cloud top altitude, and cloud top pressure level of the liquid water, and ice water cloud depending on the atmosphere profile.

	Profiles		
	US Standard (`afglus`)	Tropical (`afglt`)	Subarctic winter (`afglsw`)
	Surface temperature		
	288.2 K (14.85°C)	299.7 K (26.55°C)	257.2 K (-15.95°C)
Cirrus temperature	Cirrus altitude (km) / pressure (hPa)		
219 K (-54°C)	10.7 / 240	12.7 / 191	8.5 / 308
225 K (-48°C)	9.7 / 276	11.8 / 220	7.3 / 367
231 K (-42°C)	8.8 / 318	10.9 / 252	6.5 / 419
237 K (-36°C)	7.9 / 363	10.0 / 286	5.6 / 476
243 K (-30°C)	7.0 / 414	9.1 / 325	4.7 / 540
	Cloud top temperature for liquid cloud at 1.5 km (K / °C)		
	278.5 K / 5.35°C	290.7 K / 17.55°C	257.5 K / -15.65°C

second shape. The 'droxtal' parameterization is selected to estimate ΔF of young contrails, which primarily consist of near-spherical ice crystals (Goodman et al., 1998; Lawson et al., 1998; Gayet et al., 2012). We emphasize that contrails can be comprised of other ice crystal shapes, like single columns, hollow columns, 3D bullet rosettes, or mixtures of these (Lawson et al., 1998; Baum et al., 2005a), but the simulated shapes cover the majority of observed cirrus situations. The utilized ice optical properties of the three selected shapes are based on the parameterization from Yang et al. (2013) that assume randomly oriented ice crystals with a 'moderate' surface roughness.

– Within libRadtran clouds are defined by their geometric thickness dz, effective radius r_{eff}, and IWC. Typical IWC of contrails and in situ cirrus can range from 10^{-5} to 0.2 g m^{-3} as found during the Mid–Latitude Cirrus campaign (Luebke et al., 2016; Krämer et al., 2016, 2020). For our simulations, we span a similar range of IWC from $7 \cdot 10^{-7}$ to 0.1 g m^{-3}.

– Aircraft in situ observations of young ($t < 120$ s) contrails showed that these consist of ice crystals with diameters up to a few micrometers (Petzold et al., 1997; Sassen, 1997; Lynch et al., 2002). Shortly thereafter these ice crystals grow in size and reach ice crystal radius r_{eff} between 2 and 5 μm (Jeßberger et al., 2013; Bräuer et al., 2021). The majority of ice crystals in older ($t > 120$ s) contrails and cirrus have r_{eff} between 10 and 150 μm (Krämer et al., 2020), while mature cirrus can be composed of ice crystals with diameters larger than 150 μm (Schröder et al., 2000). The selected ice optical properties allow for simulations between 5 to 85 μm and thus cover the lower and mid range of the natural crystal size spectrum.

Within libRadtran the bulk-scattering properties of ice clouds are obtained by integrating the single-scattering properties over the entire ice crystal / particle size distribution (PSD). The PSD of an ice cloud can be approximated by a gamma

distribution (Hansen and Travis, 1974; Evans, 1998; Heymsfield et al., 2002; Baum et al., 2005a, b), which is given by:

$$n(r_{\mathrm{e}}) = N \cdot r_{\mathrm{e}}^{\mu} \cdot \exp\left(-\Lambda \cdot r_{\mathrm{e}}\right), \tag{4}$$

with $n(r_{\mathrm{e}})\mathrm{d}r$ the number of ice crystals with radii in the range of r_{e} and $r_{\mathrm{e}} + \mathrm{d}r$. N is a normalization constant such that the integral over the PSD yields the number of crystals in a unit volume (Emde et al., 2016). N itself results from the choice of the parameters in Eq. 4 that are given by the slope $\Lambda = \frac{1}{a \cdot b}$ and dispersion $\mu = \frac{1-3b}{b}$. Inserting a and b into Eq. 4 leads to:

$$n(r_{\mathrm{e}}) = N \cdot r_{\mathrm{e}}^{\left(\frac{1}{b}-3\right)} \cdot \exp\left(-\frac{r}{ab}\right), \tag{5}$$

Parameter b corresponds to the effective variance ν_{eff} (unitless), with typical values between 0.1 and 0.5 (Evans, 1998; Heymsfield et al., 2002). In libRadtran ν_{eff} is set to 0.25 (Emde et al., 2016). Parameter a corresponds to the targeted effective radius r_{eff} of the PSD. Multiple definitions for r_{eff} exist in the case of non-spherical crystals. Here we follow the definition from Yang et al. (2000), Key et al. (2002), Baum et al. (2005b), Baum et al. (2007), and Schumann et al. (2011), which describe the diameter D_{e} and radius r_{e} of a non-spherical ice crystal as:

$$D_{\mathrm{e}} = 2 \cdot r_{\mathrm{e}} = \frac{D_{\mathrm{V}}^{3}}{D_{\mathrm{A}}^{2}}, \tag{6}$$

with D_{V} the diameter of a spherical crystal with the same average volume as the ice crystal and D_{A} the diameter of a spherical crystal with the same projected area as the ice crystal. D_{A} is defined by:

$$D_{\mathrm{A}} = 2 \cdot r_{\mathrm{A}} = 2 \cdot \left(\frac{A}{\pi}\right)^{1/2} \tag{7}$$

and D_{V} is given by:

$$D_{\mathrm{V}} = 2 \cdot r_{\mathrm{V}} = \left(\frac{6 \cdot V}{\pi}\right)^{1/3}, \tag{8}$$

where V and A are the volume and the mean projected area of the ice crystal, respectively. As demonstrated by Mitchell (2002) the definition of D_{e} and r_{e} of a single crystal can be applied to a PSD, when evaluated at a bulk ice density of $917\,\mathrm{kg\,m^{-3}}$, which finally leads to:

$$r_{\mathrm{eff}} = \frac{3 \cdot \int_{L1}^{L2} V(L)n(L)\mathrm{d}L}{4 \cdot \int_{L1}^{L2} A(L)n(L)\mathrm{d}L}, \tag{9}$$

with $L1$ and $L2$ the minimum and maximum crystal size of the distribution.

The original ice optical properties from Yang et al. (2013) are processed by weighting the size dependent single-scattering phase function with the gamma distribution (Emde et al., 2016). For the gamma size distribution a minimum and maximum r_{eff} of 5 and 90 μm are selected. Parameter a in Eq. 5 is found iteratively such that the desired r_{eff} of the distribution is achieved. The obtained bulk optical properties are used for RT in the solar and the TIR wavelength range. Examples of phase functions $\mathcal{P}$ for four different crystal shapes and their characteristic features are visualized in Appendix D.

– Cloud geometric thickness dz is set to 1000 m. That represents a contrail after approximately 30 min lifetime (Freudenthaler et al., 1995) and an average cirrus or aged contrail as confirmed by climatologies from lidar (Noël and Haeffelin, 2007; Iwabuchi et al., 2012) and satellite observations, for example, by Sassen and Campbell (2001). During the cloud life time the ice crystals might grow due to supersaturation and WV deposition, and start to sediment. Sedimentation lowers the cloud base altitude and increases dz. Meerkötter et al. (1999) reported that variations in dz have only a minor impact on the cloud RE. However, to estimate the effect of varying dz a dedicated sensitivity study on dz was performed for a sub-set of the parameter range and dz of 500, 1000, and 1500 m. To investigate the effect of variations in dz on solar, TIR, and net RE, a separate sensitivity study for a sub-set of the full parameter space is performed with dz of 500 and 1500 m, while keeping the total ice water path (IWP) constant and, thus, the solar cloud optical thickness τ_{ice} constant. The total IWP and the scaled IWC are provided in Table 2. τ_{ice} can be approximated by:

$$\tau_{\text{ice}} = \frac{3 \cdot Q_{\text{e}} \cdot IWC \cdot dz}{4 \cdot \rho_{\text{ice}} \cdot r_{\text{eff}}} = \frac{3 \cdot Q_{\text{e}} \cdot IWP}{4 \cdot \rho_{\text{ice}} \cdot r_{\text{eff}}} = \frac{3 \cdot IWP}{2 \cdot \rho_{\text{ice}} \cdot r_{\text{eff}}} \tag{10}$$

with density of ice $\rho_{\text{ice}} = 917 \, \text{kg m}^{-3}$ and $Q_{\text{e}} \approx 2$ the average solar extinction efficiency factor of ice crystals (Horváth and Davies, 2007; Wang et al., 2019). It has to be noted that Eq. 10 is only applicable for the solar wavelength range.

– The parameter sensitivity study is complemented by investigating the influence of a second cloud layer. The second cloud layer is implemented as a stratiform, low-level liquid water cloud with a constant cloud top altitude $z_{\text{liq,CT}}$ at 1500 m and a geometric thickness of 500 m. The altitude of 1500 m was selected as a compromise between typical conditions of low-level stratiform clouds in the Subarctic, the mid-latitudes, and tropical regions. McFarquhar et al. (2007) and van Diedenhoven et al. (2009) found $z_{\text{liq,CT}} = 1000$ m for Arctic clouds. Slightly higher $z_{\text{liq,CT}}$ between 1000 and 1500 m are found in the mid-latitudes (Rémillard et al., 2012; Muhlbauer et al., 2014). Low-level clouds in the tropics also range between 500 and 1700 m even though some cloud tops can reach up to 2000 m (Medeiros et al., 2010; Stevens et al., 2016). Fixing $z_{\text{liq,CT}}$ at 1500 m leads to liquid cloud top temperature T_{liq} of 278.5 and 290.7 K for the mid-latitude and tropical profile, respectively. In the Subarctic profile however, T_{liq} reaches 257.2 K (-15.95 K), which is below freezing and implies a super-cooled liquid water cloud. This agrees with observations from Hogan et al. (2004) and Hu et al. (2010), who found that the majority of clouds in the Arctic ($\approx 70\,\%$) are characterized by super-cooled droplets at cloud top. Furthermore, 95 % of the observed clouds that have a T_{liq} between -15 and $0°$C have super-cooled droplets at the top. The cloud optical thickness τ_{liq} at 550 nm wavelength of the liquid water cloud is varied between 0 and 20. Within the RT simulations the optical properties of liquid water clouds are represented by pre-calculated Mie tables (Mie, 1908; van de Hulst, 1981).

An overview of the model configuration is given in Table 3 and the input parameter space is listed in Table 4. An example libRadtran input file is provided as supplementary material.

For each of the three simulated ice crystal shapes a NetCDF file is provided (Wolf et al., 2023). The files include ice cloud optical thickness τ_{ice}, the simulated upward and downward irradiances F at TOA with 120 km (with and without the presence of the ice cloud), and the calculated ice cloud radiative effect ΔF (solar, TIR, net). The available cloudy and cloud-free

Table 2. Ice water path IWP (in $g\,m^{-2}$) and ice water content IWC (in $g\,m^{-3}$) for the reference with $dz = 1000$ m and the two additional clouds with dz of 500 and 1500 m.

	IWP [$g\,m^{-2}$]						
	0.7	1.5	3	6	12	24	100
IWC (dz = 500 m) [$g\,m^{-3}$]	0.0014	0.003	0.006	0.012	0.024	0.048	0.2
IWC (dz = 1000 m) [$g\,m^{-3}$]	0.0007	0.0015	0.003	0.006	0.012	0.024	0.1
IWC (dz = 1500 m) [$g\,m^{-3}$]	0.00045	0.001	0.002	0.004	0.008	0.016	0.0667

Table 3. Basic model configuration and selected settings.

Model configuration	Selected value / setting
Radiative transfer solver	DISORT (Stamnes et al., 1988; Buras et al., 2011)
Number of streams	16
Extraterrestrial solar spectrum	Kurucz (1992)
Wavelength range	0.3–3.5 μm (solar) & 3.5–75 μm (thermal-infrared)
Molecular absorption	Gasteiger et al. (2014)
Ice properties	Yang et al. (2013)
Output altitude	120 km = TOA

Table 4. Simulated parameter space.

Model parameter	Symbol	Simulated values	Total number of combinations
Solar zenith angle (°)	θ	0, 10, 30, 50, 70, 85	6
Ice water content ($g\,m^{-3}$)	IWC	0.0007, 0.0015, 0.003, 0.006, 0.012, 0.024, 0.1	7
Crystal effective radius (μm)	r_{eff}	5, 10, 15, 25, 60, 85	6
Cirrus temperature (K)	$T_{\mathrm{cld,ice}}$	219, 225, 231, 237, 243	5
Surface albedo	α_{srf}	0, 0.15, 0.3, 0.6, 1.0	5
Surface temperature (K)	T_{srf}	257.2, 288.2, 299.7	3
Atmosphere profiles	-	US Standard atmosphere `afglus`, tropical `afglt`, subarctic winter `afglsw`	-
Second cloud layer optical depth	τ_{liq}	0, 1, 5, 10, 20	5
Ice crystal shapes	-	aggregates (8–column-aggregates), droxtals, plates	3
			283,500

Table 5. List of variables that are provided in the NetCDF. The output is provided at top of atmosphere located at 120 km altitude.

Long name	Symbol	Variable name in NetCDF file	Unit
Dimensions			
Solar zenith angle	θ	*solar_zenith_angle*	°
Ice cloud temperature	T_{ice}	*ice_cloud_temp*	K
Surface albedo	α_{srf}	*surface_albedo*	-
Ice water content	IWC	*ice_water_content*	$\mathrm{g\,m^{-3}}$
Surface temperature	T_{srf}	*surface_temperature*	K
Ice crystal effective radius	r_{eff}	*crystal_effective_radius*	μm
Liquid water cloud optical thickness	τ_{liq}	*optical_thickness_liquid_water_cloud*	-
Cloud fraction	-	*cloud_fraction*	-
Variables			
Downward solar total (direct + diffuse) irradiance	$F^{\downarrow}_{\mathrm{sol}}$	*Fdn_sol*	$\mathrm{W\,m^{-2}}$
Upward solar irradiance	$F^{\uparrow}_{\mathrm{sol}}$	*Fup_sol*	$\mathrm{W\,m^{-2}}$
Downward thermal-infrared irradiance	$F^{\downarrow}_{\mathrm{tir}}$	*Fdn_tir*	$\mathrm{W\,m^{-2}}$
Upward thermal-infrared irradiance	$F^{\uparrow}_{\mathrm{tir}}$	*Fup_tir*	$\mathrm{W\,m^{-2}}$
Solar cloud radiative effect	ΔF_{sol}	*RF_sol*	$\mathrm{W\,m^{-2}}$
Thermal-infrared cloud radiative effect	ΔF_{tir}	*RF_tir*	$\mathrm{W\,m^{-2}}$
Net radiative effect	ΔF_{net}	*RF_net*	$\mathrm{W\,m^{-2}}$
Ice cloud optical thickness	τ_{ice}		-

irradiances further allow to calculate the cirrus RE by scaling the 'cloudy' RE with the required cloud cover. An overview of all variables provided in the NetCDF files are given in Table 5. The data set allows the user to extract ΔF values for their parameter combinations, instead of running costly RT simulations. The look-up-table could in fact be coupled with models of any complexity, as long as they simulate the dimensions of the data set, namely: solar zenith angle, ice cloud temperature, surface albedo, ice water content, surface temperature, ice crystal effective radius, and liquid water cloud optical thickness.

The simulations base on three relative humidity profiles, which were selected to represent subarctic, mid-latitude, and tropical conditions. An estimation in RE variability due to variations in the RH profile showed an effect of less than 1 % for ΔF_{sol} but can range up to 4 % for ΔF_{tir} and 8 % for ΔF_{net} especially for the warm and moist tropical profile. These variations have to be considered, when using the data set. We further emphasizes that the simulations are performed with a 1D RT solver, i.e., plane-parallel clouds, that neglect 3D scattering and horizontal photon transport (Gounou and Hogan, 2007).

2.3 Relationship between effective radius, ice water content, crystal number concentration, and cloud optical thickness

The liquid water content (LWC) of a liquid water cloud can be obtained by:

$$\text{LWC} = \frac{4}{3} \cdot \pi \cdot \rho_{\text{liq}} \cdot \int_0^\infty n(r) \cdot r^3 \cdot \mathrm{d}r, \tag{11}$$

with $\rho_{\text{liq}} = 1000 \,\text{kg}\,\text{m}^{-3}$ the density of liquid water, r the radius, and $n(r)$ the number of droplets with size r. Equation 11 assumes spherical ice crystals, so might be valid for droxtals, which are almost spherical ice crystals, but it is invalid for other ice crystal shapes. To obtain the particle number concentration N_{ice} for non-spherical crystals, appropriate power-law mass-dimension relations are needed. Here we employ Eq. 29 from Mitchell et al. (2006) but modify the notation to be consistent with the previous equations from the present study. Equation 29 from Mitchell et al. (2006) is then given by:

$$\text{IWC} = \frac{\alpha \cdot \Gamma(\beta + \mu + 1) \cdot N_{\text{ice}}}{\Gamma(\mu + 1) \cdot \Lambda^\beta}, \tag{12}$$

with Γ the result of the numerically solved gamma function. The constants α and β are the prefactor and the power in the mass–dimensional relationship, respectively. They are related by:

$$m = \alpha \cdot D^\beta, \tag{13}$$

with m the mass of the ice crystal and D the maximum dimension of the ice crystal. Both constants depend on the ice crystal shape and are, for example, listed in Mitchell (1996). Using Eq. 13 and assuming an exponential PSD with the special case $\mu = 0$ and $\Lambda = \frac{3}{r_e}$ (Deirmendjian, 1962; Petty and Huang, 2011), finally leads to:

$$N_{\text{ice}} = \frac{3^\beta \cdot \text{IWC}}{\alpha \cdot \Gamma(\beta + 1) \cdot r_e^\beta}. \tag{14}$$

Therefore N_{ice} is proportional to $\frac{\text{IWC}}{r_e^\beta}$, with β around 2 for aggregates, 2.4 for hexagonal-plates, and 3 for almost spherical droxtals (Mitchell, 1996).

2.4 Approximation of radiative transfer in the thermal-infrared

Radiation in the TIR is primarily of terrestrial origin (Glickman, 2000). Therefore, the TIR irradiance at the TOA has only an upward directed component $F^{\uparrow,\text{TIR}}$, while the downward component $F^{\downarrow,\text{TIR}}$ is essentially zero. The magnitude of $F^{\uparrow,\text{TIR}}$ is primarily driven by the cloud absorption optical depth, the surface temperature T_{srf}, and the (ice) cloud temperature $T_{\text{cld,ice}}$ or ice cloud altitude z_{ice} (Corti and Peter, 2009). Assuming the Earth surface is a black body, the outgoing $F_{\text{TIR}}^{\uparrow}$ at TOA could be calculated, in a first order approximation, by the Stefan–Boltzmann-law:

$$F_{\text{cf}}^{\uparrow} = \sigma \cdot \epsilon \cdot T^4, \tag{15}$$

which is obtained by integrating the Planck function over all wavelengths and 2π of a hemispheric solid angle. In Eq. 15 the Stefan–Boltzmann-constant is represented by $\sigma = 5.67 \cdot 10^{-8} \mathrm{W\,m^{-2}\,K^{-4}}$ and the emissivity $\epsilon = 1$ of a blackbody. In reality however, the Earth acts as a gray-body ($\epsilon \neq 1$) and the surrounding atmosphere must be taken into account.

Absorption of radiation in the atmosphere in the TIR wavelength range depends on wavelength and atmospheric composition. The primary components that control absorption are water vapor and carbon dioxide (CO_2) (Liou, 1992). While CO_2 is well-mixed and thus approximately constant in space and time, WV is highly variable. Furthermore, the amount of WV is linked to the temperature in the AP via the Clausius–Clapeyron-equation (Corti and Peter, 2009). The lowermost values of the AP are also influenced by T_{srf}. Due to these interactions, Corti and Peter (2009) developed a model to estimate TIR irradiances and the resulting CRE. The model was derived by fitting RT simulations, which cover a wide range of environmental conditions, to Eq. 15, which leads to:

$$F_{\mathrm{cf}}^{\uparrow *} \approx \sigma^* \cdot \epsilon \cdot T_{\mathrm{srf}}^{k^*}, \tag{16}$$

with $\sigma^* = 1.607 \cdot 10^{-4} \mathrm{W\,m^{-2}\,K^{-2.528}}$ and $k^* = 2.528$. $F_{\mathrm{cf}}^{\uparrow *}$ represents surface surface emission with T_{srf} and atmospheric absorption.

Clouds in the atmosphere can be approximated by semi-transparent blackbodies that partly absorb and re-emit radiation according the Stefan–Boltzmann-law. The emissivity ϵ of a cloud depends on τ, which in turn depends on the wavelength (Stephens et al., 1990). $F_{\mathrm{TIR}}^{\uparrow}$ in the cloudy case can be estimated with:

$$F_{\mathrm{TIR}}^{\uparrow} = (1 - \epsilon^*) \cdot \sigma^* \cdot T_{\mathrm{srf}}^{k^*} + \epsilon^* \cdot \sigma^* \cdot T_{\mathrm{cld}}^{k^*}, \tag{17}$$

with σ^* and k^* for cloud-free conditions. ϵ can be approximated by

$$\epsilon \approx 1 - \exp{-\delta \cdot \tau}, \tag{18}$$

where $\delta = D \cdot (1 = \tilde{\omega})$ and $D \approx 1.66$, relying on the zero-scattering assumption (Stephens et al., 1990), and an effective emissivity ϵ^* that is also derived from their RT simulations. Finally, the TIR RE of a cloud above a surface can be approximated with:

$$\Delta F_{\mathrm{tir}} = F_{\mathrm{TIR,c}} - F_{\mathrm{TIR,cf}} \approx$$
$$\sigma^* (T_{\mathrm{srf}}^{k^*} - T_{\mathrm{cld}}^{k^*}) \cdot (1 - \exp{(-\delta^* \cdot \tau)}), \tag{19}$$

with $\delta^* = 0.75$. It follows from Eq. 19 that the forcing of a cloud, with constant τ, is proportional to the temperature difference between cloud and surface.

3 Results

We first provide an overview of how r_{eff} and IWC determine the cloud optical and microphysical properties. Figure 1a–d illustrates the dependence of N_{ice} and τ_{ice} as a function of r_{eff} and IWC. N_{ice} is approximated by Eq. 14, assuming droxtals
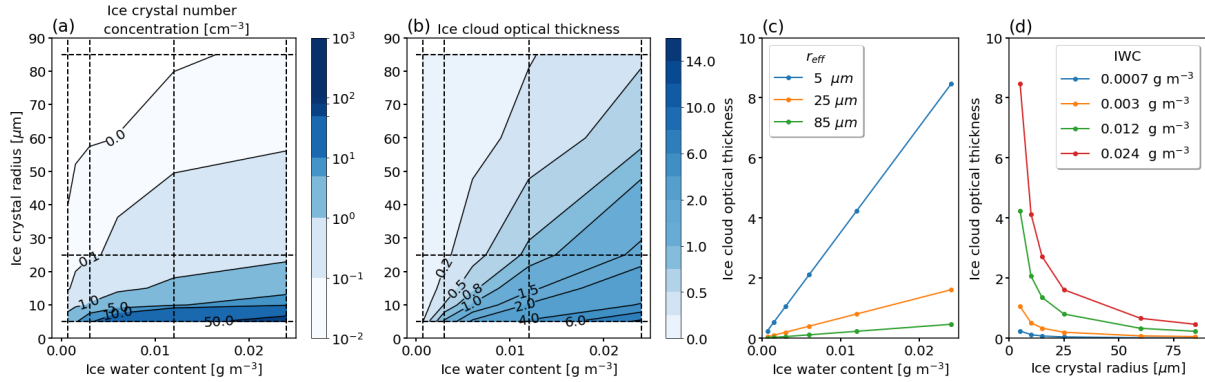
Figure 1. (a–b) Calculated ice crystal number concentration N_{ice} (in cm^{-3}) and simulated cloud optical thickness τ_{ice} at 550 nm wavelength as a function of ice water content IWC (in g m^{-3}) and effective crystal radius r_{eff} (in μm). A cloud geometric thickness dz of 1000 m is selected. **(c–d)** Cross-sections along lines of constant r_{eff} or IWC that are indicated as dashed lines in panel a and b, respectively.

(almost spherical ice crystals), a mono-disperse particle size distribution, and a cloud geometric thickness dz of 1000 m. The ice cloud optical thickness τ_{ice} at 550 nm wavelength is directly obtained from the libRadtran verbose output using optical properties of droxtals. The largest N_{ice} values result from the smallest ice crystals sizes ($r_{eff} < 10$ μm), particularly

300 in combination with large IWC (Fig. 1a). For combinations of small $r_{eff} < 15$ μm and large IWC, N_{ice} is most sensitive to r_{eff}, which is indicated by the narrowing contour lines that align along the x-axis. For a constant r_{eff} of 5 μm, the estimated N_{ice} ranges from 1 to over 80 cm^{-3}. Such concentrations of $N_{ice} > 80$ cm^{-3} are rarely observed in natural cirrus though they can occur in very young contrails and contrail-induced cirrus (Krämer et al., 2016). Generally smaller N_{ice} and a reduced sensitivity to r_{eff} and IWC is found for $r_{eff} > 20$ μm, where N_{ice} mostly ranges below 10 cm^{-3}.

305 The inherent dependencies of N_{ice} presented in Fig. 1a are also found in the distribution of the ice cloud optical thickness τ_{ice} at 550 nm shown in Fig. 1b. Following lines of constant r_{eff} (Fig. 1c), the increase in IWC corresponds to a linear increase in N_{ice} and, therefore, to a gain in the total scattering and absorption particle cross-sections. The absorption of radiation by liquid water and ice (as characterized by the complex refractive index) at 550 nm wavelength is weak and, therefore, scattering dominates τ_{ice}. Alternatively, going along lines of constant IWC towards larger r_{eff} leads to a decrease in N_{ice} and a related

310 decrease of the total scattering particle cross-section (cloud albedo effect, Fig. 1d). This effect is most effective for larger IWC (optically thick clouds) and is less pronounced for clouds with smaller IWC.

To reduce the multi-dimensionality, for each of the eight parameters a reference is defined by selecting either the minimum or maximum value from the parameter space. The reference parameters are selected to highlight the upper or lower range of each parameter and the spanned variation, and to define the reference for the fixed parameters. The reference parameters are

315 given by $\theta = 0°$, $T_{cld,ice} = 219$ K, $\alpha_{srf} = 0$, $T_{srf} = 299.7$ K, $r_{eff} = 85$ μm, and $\tau_{liq} = 0$ (no liquid water cloud). For IWC we use an intermediate value of 0.024 g m^{-3} because together with a dz of 1000 m and an r_{eff} of 85 μm this leads to a τ_{ice} of 0.46 at 550 nm wavelength, which is representative for contrails and young cirrus (Iwabuchi et al., 2012). Otherwise electing

the minimum or maximum IWC in combination with r_{eff} of 85 μm would lead to high or low τ_{ice} that are not representative for contrails. For ice crystal shape, we select aggregates as the reference. We particularly emphasize that the defined references are not representative of any particular cloud situation, but are a useful point of comparison to assess the impact of a given parameter on the diversity of cloud RE.

Using the defined reference, Fig. 2a–c shows solar, TIR, and net ΔF, respectively (similar to Meerkötter et al. (1999)). First, the influence of variations in θ is investigated in order to sample the diurnal cycle and its variation as a function of latitude. For all Sun geometries, ΔF_{sol} is negative and, therefore, the cirrus has a cooling effect in the solar spectrum on the atmosphere-surface system. ΔF_{sol} intensifies (i.e., becomes more negative) with increasing θ as the length of the optical path through the cloud, $s = \Delta z / \cos\theta$, increases, which is accompanied by enhanced scattering (and thus upward directed scattering) of the incoming radiation (Wendisch et al., 2005). In addition, a lower fraction of the incident radiation is scattered towards the surface but scattered upward to space. This is due to the strong forward peak in the ice crystal phase function $\mathcal{P}$ that decreases sharply for $\Theta > 10°$ (see in Appendix Fig. D1). An exception appears for θ of 85°, where ΔF_{sol} is smallest. Variations in θ lead to ΔF_{sol} between -55.9 and -27.5 W m^{-2}. As expected, ΔF_{tir} is unaffected by the Sun position with a constant ΔF_{tir} = 46.0 W m^{-2}. The resulting sensitivity of ΔF_{net} is driven by ΔF_{sol} with ΔF_{net} between -9.9 and 18.5 W m^{-2}. During nighttime there is no contribution from ΔF_{sol} leading to a constant, positive ΔF_{net} = 46.0 W m^{-2} (leading to a warming).

As expected, variations in r_{eff} have the largest effect on the solar, TIR, and net ΔF, as N_{ice} relates to r_{eff} by the power of $-\beta$, which depends on the ice crystal shape (see Sec. 2.3 and Eq. 14). Increasing r_{eff} from 5 to 85 μm leads to ΔF_{sol} between -599.5 and -50.2 W m^{-2}. The distribution of ΔF_{tir} has a minimum and maximum of 46.0 and 149.8 W m^{-2}, respectively. ΔF_{sol} dominates ΔF_{tir} and results in values of ΔF_{net} ranging from -449.8 to -4.2 W m^{-2}.

Variations in IWC affect solar, TIR, and net ΔF. Generally, an increase in IWC (increase in τ_{ice} for fixed r_{eff}), enhances total scattering and absorption particle cross-sections and, therefore, intensifies the cooling in the solar (more negative ΔF, cloud albedo effect) and the TIR heating (more positive ΔF). ΔF_{sol} ranges from -191.1 to -1.5 W m^{-2}, with ΔF_{sol} = -50.2 W m^{-2} obtained for the reference IWC. The distribution of ΔF_{tir} spans values between 1.8 and 112.7 W m^{-2}, leading to ΔF_{net} from -78.4 to 1.1 W m^{-2}. The ΔF given above correspond to a varying IWC and assume r_{eff} = 85 μm. For smaller r_{eff} ΔF increases and thus increases the range of solar, TIR and net ΔF. In addition, the IWC becomes dominant over r_{eff} in Fig. 2, when selecting a reference with smaller r_{eff}.

Variations in α_{srf} impact only the solar spectrum, as expected, with ΔF_{sol} between -50.2 and 15.4 W m^{-2}. The most negative RE appears over non-reflective surfaces and decreases with increasing α_{srf}, due to the decrease in contrast between the surface and the cirrus. In cases where α_{srf} exceeds the cloud albedo, ΔF_{sol} becomes positive. For the optical thin reference this is the case over a fully sea ice covered area with $\alpha_{\mathrm{srf}} \approx 1$. The TIR component remains almost unaffected with ΔF_{tir} between 39.5 and 46 W m^{-2}. Together with the decreasing cooling effect in the solar, the warming in the TIR mostly dominates and leads to ΔF_{net} ranging between -4.2 and 55.0 W m^{-2}.

The influence of a varying surface temperature T_{srf} or cirrus temperature $T_{\mathrm{cld,ice}}$ (related to cloud base altitude), are investigated for a cloud scenario with a solar surface albedo α_{srf} set to 0. Varying surface temperature T_{srf} or cirrus temperature $T_{\mathrm{cld,ice}}$ (related to cloud base altitude), ΔF_{sol} remains almost constant with a minimum and maximum ΔF_{sol} for both param-
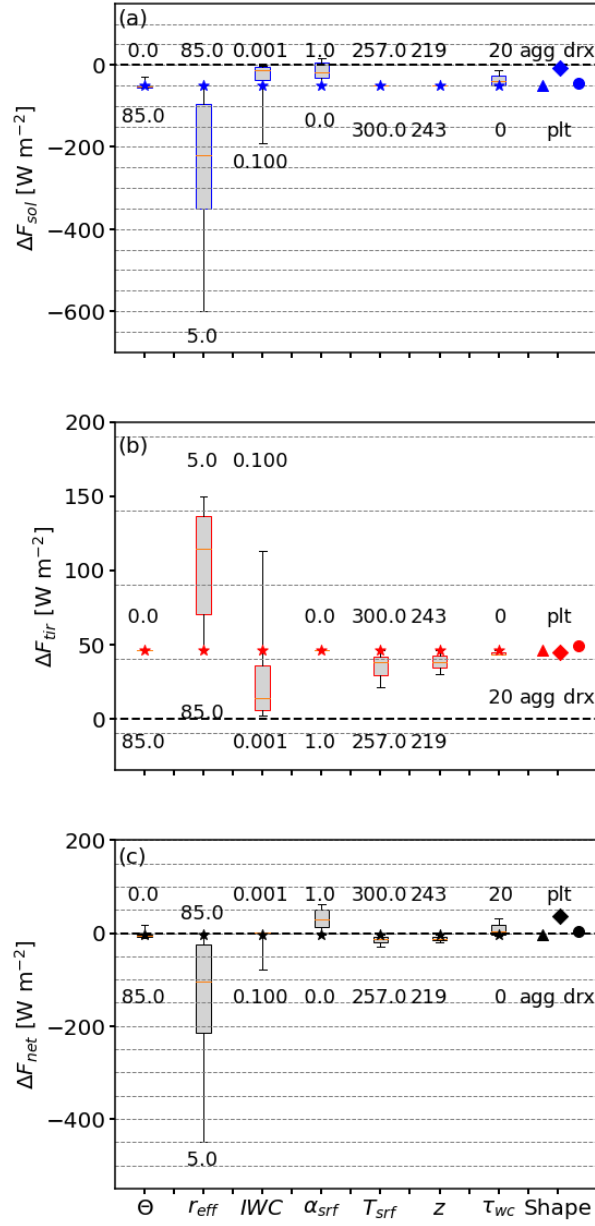
Figure 2. (a–c) Box and whisker plot of solar, TIR, and net ΔF (in W m^{-2}) due to the variation of the parameters indicated as the x-axis. The boxes represent the $25^{\text{th}}-$ and 75th-percentiles, while the whiskers indicate the minimum and maximum values. Median values are given in each box by horizontal, orange lines. The stars indicate the reference with solar zenith angle $\theta = 0°$, effective radius $r_{\text{eff}} = 85$ μm, ice water content IWC $= 0.024$ g m^{-3}, surface albedo $\alpha_{\text{srf}} = 0$, surface temperature $T_{\text{srf}} = 299.7$ K, ice cloud temperature $T_{\text{cld,ice}} = 219$ K, and liquid water cloud optical thickness $\tau_{\text{liq}} = 0$. Minimum and maximum of the parameter ranges are given by the numbers. Plot idea adapted from Meerkötter et al. (1999).

eters of -50.2 and -49.2 W m^{-2}, respectively. These small differences are due to changes in molecular absorption, which results from the variations in the relative humidity profile as the profile depends on the selected T_{srf}. A noticeable effect is found for ΔF_{tir}, which is impacted by variations in $T_{\mathrm{cld,ice}}$ and T_{srf}. While decreasing $T_{\mathrm{cld,ice}}$ from 243 to 219 K lowers ΔF_{tir} from 46 to 29.9 W m^{-2}, a decrease in T_{srf} from 300 to 257 K reduces ΔF_{tir} from 46 to 20.8 W m^{-2}. Consequently, ΔF_{tir} determines the response of the resulting ΔF_{net}, which spans from -4.2 to -19.4 W m^{-2} for $T_{\mathrm{cld,ice}}$ and -28.7 to -4.2 W m^{-2} for T_{srf}. The greater influence of T_{srf} on ΔF_{tir} and ΔF_{net} is explained simply by the greater variation of the input.

A second cloud layer is considered by inserting a liquid water cloud with a cloud top altitude $z_{\mathrm{base}} = 1500$ m and a geometric thickness $\mathrm{d}z = 500$ m. Figure 2 shows that this second cloud influences both components ΔF_{sol} and ΔF_{tir}. Generally speaking, the liquid water cloud enhances the fraction of solar, upward directed radiation compared to a dark surface. With increasing τ_{liq} (increase in LWC) $\alpha_{\mathrm{cld,ice}}$ exceeds α_{srf}, which lowers the albedo contrast between the ice cloud and the surface for most of the parameter combinations. This minimizes solar RE and leads to a minimum of -51.1 W m^{-2} and a maximum of -11.6 W m^{-2}. For the TIR part the increase in LWC masks the influence of the underlying surface by absorbing the upward TIR radiation from the surface and re-emitting radiation at the liquid water cloud temperature. This leads to ΔF_{tir} between 43.2 and 46.0 W m^{-2}. The resulting ΔF_{net} is characterized by a minimum and maximum of -6.5 and 31.6 W m^{-2} primarily impacted by the solar component.

The parameter study is complemented by investigating the effect of prescribing three different ice crystal shapes. The variation in ΔF_{sol} due to the transition from almost spherical (droxtals) to non-spherical crystals (aggregates) leads to a relative change in ΔF_{sol} that is, in terms of RE, comparable to a variation in θ. The strongest cooling effect (negative ΔF_{sol}) is found for aggregates with -50.2 W m^{-2} and decreases for droxtals and plates to -44.3 and -8.6 W m^{-2}, respectively. Ice crystal shape also impacts ΔF_{tir}. Aggregates lead to ΔF_{tir} of 46 W m^{-2}, while plates and droxtals can cause a ΔF_{tir} of 44.5 and 48.9 W m^{-2}, respectively. Consequently, the largest ΔF_{net} with 35.8 W m^{-2} is found for plates and followed, in decreasing order, by droxtals and aggregates with 4.5 and -4.2 W m^{-2}, respectively. As mentioned in the introduction, the uncertainty in the ice crystal shape causes uncertainties in the calculated ΔF. Nevertheless, using three different ice crystal shapes for the irradiance simulations shows that the shape-specific scattering properties are of lesser importance compared to other parameters like the ice crystal size (distribution), the IWC, or surface properties.

The presented analysis of solar, TIR, and net ΔF sensitivity on the selected input parameters generally agrees with the results from Meerkötter et al. (1999). We found differences in the importance of the parameters, which are explained by the fact that our simulations span a larger and different parameter range, for example in r_{eff}, IWC, and T_{srf}. Selecting cloud parameters ($\theta = 30°$, $T_{\mathrm{cld,ice}} = 231$ K, $\alpha_{\mathrm{srf}} = 0.15$, $T_{\mathrm{srf}} = 288$ K, $r_{\mathrm{eff}} = 10\ \mu$m, and $\tau_{\mathrm{liq}} = 0$) whether case A in (Meerkötter et al., 1999), we find that the IWC becomes the driving parameter, which then agrees with the results from Meerkötter et al. (1999). However, a more quantitative comparison between Meerkötter et al. (1999) is difficult as the parameters that best match are not identical. Even by choosing similar cloud parameters, by matching the IWP and selecting r_{eff} to yield $\tau_{\mathrm{ice}} \approx 0.52$, the simulated clouds and cloud case A from Meerkötter et al. (1999) differ in $\mathrm{d}z$, which impacts ΔF_{sol} and ΔF_{tir} with different intensity.

It is further emphasized that the presented ΔF_{net} is representative for daytime situations only, when the Sun is above the horizon. In the absence of solar illumination during nighttime, the net effect is entirely determined by and equal to ΔF_{tir}, which is positive (warming effect) in all simulation cases. Accordingly, all simulated cloud cases do have a net warming effect at night. For a more in-depth analysis, the subsequent plots focus on the impact of each individual parameter.

3.1 Sensitivity on ice crystal shape

One difficulty of RT simulations in ice clouds is the uncertainty about the dominating ice crystal shape, which is commonly unknown and, therefore, a general ice crystal shape has to be assumed (Kahnert et al., 2008). Scattering and absorption by an ice crystal is characterized by its orientation, complex refractive index of ice, the wavelength of the incident light, shape, size, and the resulting asymmetry parameter. The asymmetry parameter is a measure of the asymmetry of the phase function $\mathcal{P}$ between forward and backward scattering (Macke et al., 1998; Fu, 2007). $\mathcal{P}$ provides the angular distribution of the scattered direction in relation to the incident light. For example, in case of idealized hexagonal ice crystals and wavelength below 1.4 μm, the asymmetry parameter is primarily determined by the ice crystal shape / aspect ratio but for wavelength larger then 1.4 μm the asymmetry parameter also depends on the ice crystal size (Fu, 2007; Yang and Fu, 2009; van Diedenhoven et al., 2012). Consequently, the assumption of an ice crystal habit and ice crystal size, with related aspect ratio, are vital information to estimate the ice cloud RE. Furthermore, the ice optical properties by Yang et al. (2010, 2013), which are used for the RT simulations in the present study, based on a coupling of the maximum diameter of the ice crystal and the aspect ratio, with the later one being different for each crystal shape. This impacts the RT of different ice clouds with varying IWC and r_{eff}.

Subsequently, the shape-effect is quantified using Eq. 20 and relative differences in ΔF are given with respect to crystals with the same r_{eff} in relation to the ΔF simulated for aggregates. Figure 3a–c show ΔF_{sol} as a function of IWC, separated for crystal shape, r_{eff}, and three selected θ. For simplicity α_{srf} and τ_{liq} are set to zero in this discussion.

The strongest ΔF_{sol} is found for aggregates (green) with $r_{\text{eff}} = 5 \, \mu$m with the Sun at zenith ($\theta = 0°$, Fig. 3a). A lower cooling effect in the solar spectrum is found for droxtals (orange) and plates (blue) with same r_{eff}. The order of ΔF_{sol} remains constant for increasing r_{eff}.

The spread in ΔF_{sol} across crystal shapes with the same r_{eff} and IWC can be interpreted as a potential uncertainty in ΔF_{sol} due to the ice crystal shape. One has to keep in mind that the differences partially result from deviating crystal size distributions as these depend on the selected crystal shape. Macke et al. (1998) showed that, in the solar wavelength range, the crystal shape is the main driver and the actual ice PSD has only a minor effect on ΔF_{sol}. Nevertheless, Mitchell (2002) and Mitchell et al. (2011) found that the PSD also has a considerable impact on ΔF_{tir}, leading to differences of up to 48% in the single-scattering albedo, when switching between PSD.

To quantify the deviations resulting from the ice crystal shape, Fig. 3d–f show absolute and Fig. 3g–i present relative differences of ΔF_{sol} of droxtals and plates with respect to aggregates. For $\theta = 0°$ the largest absolute deviation is found for plates with r_{eff} of 25 μm and highest IWC with an absolute range of up to 250 W m^{-2} ($r_{\text{eff}} = 25 \, \mu$m, $\theta = 0°$, $\tau_{\text{ice}} = 6.6$), corresponding to a relative difference of 58 %. Relative deviations reach even larger values, e.g., when the cloud is optically thinner and ΔF_{sol} gets smaller. In case of plates the relative deviations range from -20% ($r_{\text{eff}} = 5 \, \mu$m) to -82% ($r_{\text{eff}} =$
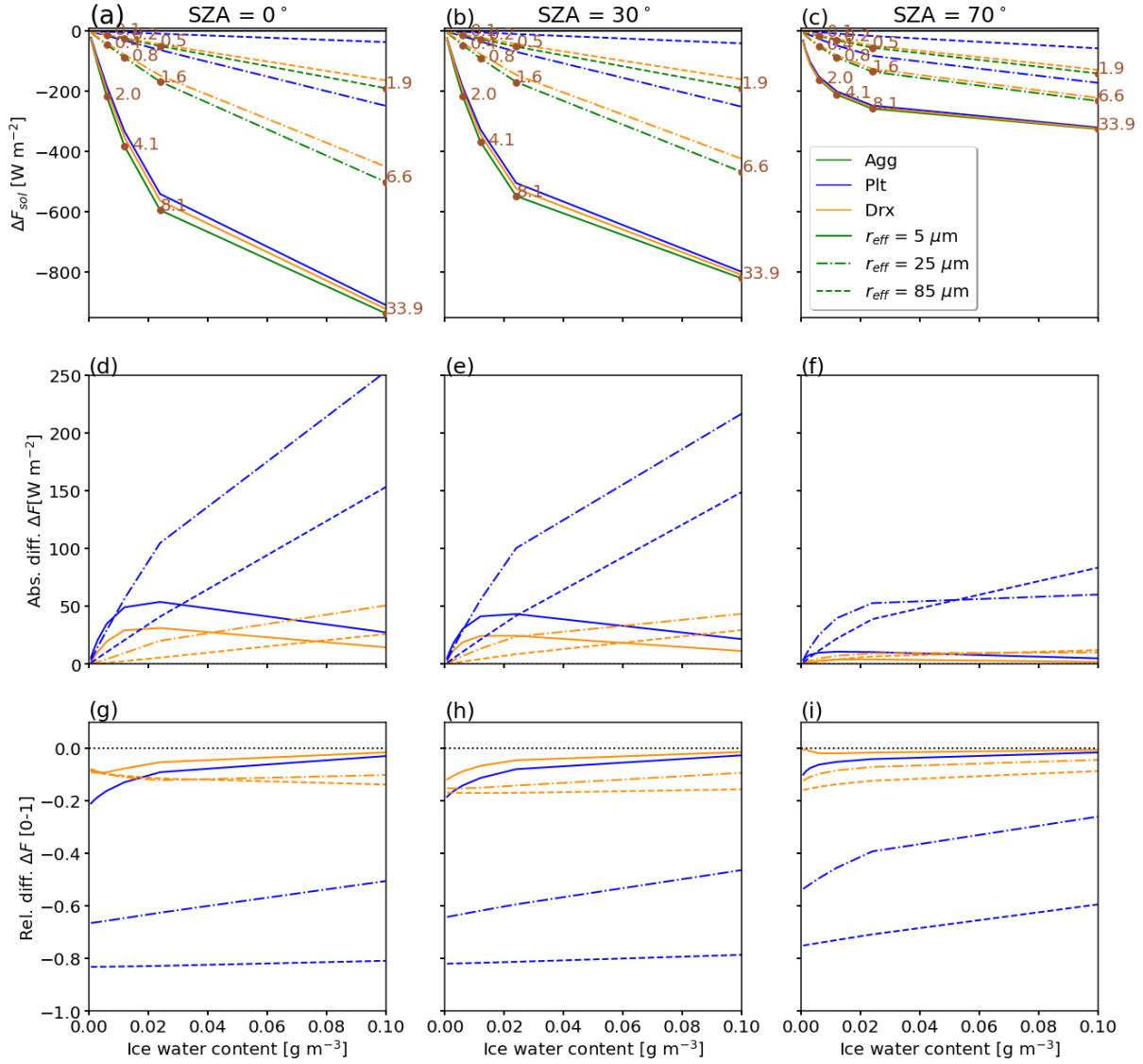
Figure 3. (a–c) Solar radiative effect ΔF_{sol} (in W m^{-2}) as a function of ice water content IWC for three values of solar zenith angle θ of $0°$, $30°$, and $70°$. Three ice crystal radii r_{eff} of 5 (solid), 25 (dash-dot), and 85 μm (dashed) are indicated. The ice crystal shape is color-coded with aggregates 'Agg', plates 'Plt', and droxtals 'drx' given in green, blue, and orange, respectively. **(d–f)** show absolute difference and **(g–i)** relative difference between ΔF_{sol} of droxtals and plates with respect to aggregates with the same crystal radius. The numbers indicate the optical thickness simulated for the reference that contains ice aggregates.

85 μm). The large absolute and relative deviations between plates and aggregates in ΔF_{sol} and later ΔF_{net} appear because plates are characterized by the smallest reflectance and absorption efficiency (Key et al., 2002; Yang et al., 2005). The absolute differences among droxtals and aggregates are smaller. With increasing IWC the absolute ranges quickly reach a maximum of 27 W m^{-2} at IWC of 0.024 g m^{-3} and decrease towards the largest IWC. The associated relative deviations are also smaller

425   compared to plates, ranging between $-3\,\%$ ($r_{\mathrm{eff}} = 5\ \mu$m) and $-18\,\%$ ($r_{\mathrm{eff}} = 85\ \mu$m).

       Another characteristic of the absolute range of ΔF_{sol} is the steep slope for $\theta = 0°$ over the entire range of IWC. For illumination geometries with the Sun closer to the horizon, particularly $\theta = 70°$, the behavior of absolute range in ΔF_{sol} is characterized by a rapid increase and convergence towards a maximum. At a certain IWC and related τ_{ice}, the slant optical path and cloud-radiation interactions are dominated by multiple scattering that suppresses single-scattering effects of individual ice

430   crystal shape, hence, reducing the absolute and relative difference resulting from the choice of the ice crystal shape. This is supported by earlier observations and simulations for example by Wendisch et al. (2005), who showed that for large θ and multiple-scattering the shape effect becomes less prominent.

       Next, we consider the solar, TIR, and net ΔF at $\theta = 30°$ (Fig. 4). The left most column for ΔF_{sol} is identical to the middle column in Fig. 3. In the TIR, the largest ΔF_{tir} is generally found for smallest crystals (5 μm) and highest IWC in decreasing

435   order from droxtals, plates, and aggregates. With increasing crystal size the order changes to droxtal, aggregates, and plates, and the absolute values of ΔF_{tir} decrease. The largest ΔF_{tir} range of 130 W m^{-2} is found for clouds with IWC between 0.024 and 0.1 g m^{-3} caused by droxtals. For thin clouds with IWC < 0.04 g m^{-3} the largest absolute range $R_{\Delta F,\mathrm{tir}}$ of around 6.5 W m^{-2} appears for r_{eff} of 5 and 25 μm, which is shifting towards larger IWC with increasing r_{eff} and vanishes for the largest crystals with r_{eff} of 85 μm. The relative differences are largest for the optically thinnest clouds and decrease with

440   increasing IWC. While droxtals are characterized by relative differences close to 0 % ($r_{\mathrm{eff}} = 5\ \mu$m; IWC = 0.1 g m^{-3}) and 18 % ($r_{\mathrm{eff}} = 25\ \mu$m; IWC = 0.007 g m^{-3}), plates lead to relative differences between 9 % ($r_{\mathrm{eff}} = 5\ \mu$m; IWC = 0.007 g m^{-3}) and $-5\,\%$ ($r_{\mathrm{eff}} = 85\ \mu$m, IWC 0.007 g m^{-3}). The TIR RE of the optically thickest cloud is independent on ice crystal shape, which is addressed to multiple scattering.

       For all IWC and r_{eff}, ΔF_{sol} is generally larger than ΔF_{tir} and, therefore, dominates resulting ΔF_{net} (Figure 4c, f). Con-

445   sequently, ΔF_{net} and absolute ranges among the ice crystal shapes follow the distributions from ΔF_{sol}. The largest relative deviations are found for the optically thinnest clouds, where ΔF_{net} is generally small. In these cases of optically thin clouds consisting of the smallest crystals ($r_{\mathrm{eff}} = 5\ \mu$m) the relative deviations exceed the relative difference for optically thick clouds with the same crystal size by a factor of 10.

       The analysis of all simulations shows that the crystal shape assumption on the cirrus RE is small compared to other pa-

450   rameters particularly IWC or r_{eff} (see Fig 2). However, we found a larger variability in ΔF_{sol} and the resulting ΔF_{net}, i.e., weather a contrail has a net warming or cooling effect compared to ΔF_{tir}. For the defined reference consisting of aggregates, a ΔF_{sol} of -50.2 W m^{-2} was simulated, while for plates and droxtals values of ΔF_{sol} of -8.6 and -44.3 W m^{-2} were obtained, respectively. The impact of the crystal shape is less pronounced in the TIR wavelength range with ΔF_{tir} of 46, 44.5, and 48.9 W m^{-2} for aggregates, plates, and droxtals, respectively. The variation of ΔF_{sol} propagates into ΔF_{net} with -4.2, 35.9

455   and 4.6 W m^{-2} for aggregate, plates, and droxtals, respectively. Based on the presented simulations, we found larger maximum
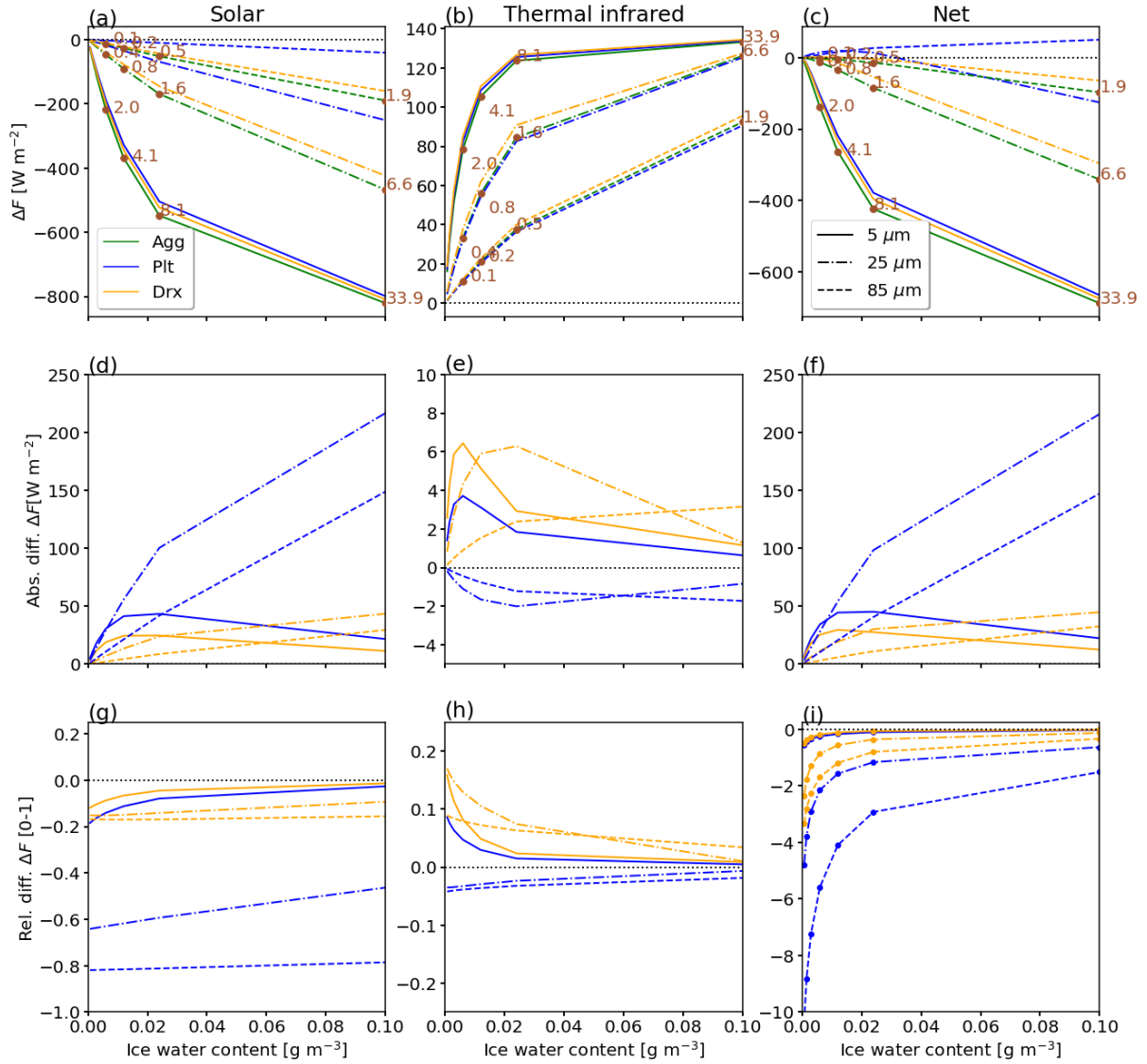
Figure 4. Same as Fig. 3 but for solar zenith angle $\theta = 30°$, and ΔF_{sol} (left), ΔF_{tir} (middle), and ΔF_{net} (right).

variations in ΔF_{sol}, ΔF_{tir}, and ΔF_{net} of 41.6, 4.4, and 40 W m^{-2}, respectively, compared to Meerkötter et al. (1999). They found variations in ΔF_{sol}, ΔF_{tir}, and ΔF_{net} of 2, 6, and 7 W m^{-2}, respectively. The difference are explained by the selected reference (Meerkötter et al., 1999). However, selecting cloud parameters similar to the reference cloud of Meerkötter et al. (1999), we still found larger maximum variations ΔF_{sol}, ΔF_{tir}, and ΔF_{net} of 17.3, 4.2, and 17.9 W m^{-2}, respectively. This is
460   attributed to the remaining differences among the selected reference values.

3.2   Sensitivity on solar zenith angle and surface albedo

In this section the impact of each parameter is estimated by fixing one parameter at a time (represented by the x-axis), while the others can vary. For example, in case of θ, all simulations, for steps of θ given in Table 4, are extracted from the 8-D hypercube. The extracted sub-sample, in the example for a specific θ, is used to calculate and visualize the distributions of solar, TIR, and
465   net ΔF. This strategy can be interpreted as a type of sub-sampling, by averaging all unfixed parameters to project ΔF onto the one-dimensional space. The impact of each parameter is further quantified by the minimum and maximum RF. We define the full range of ΔF by:

$$R_{\Delta \mathrm{F}} = max\{\Delta F\} - min\{\Delta F\}, \tag{20}$$

with $max\{\Delta F\}$ and $min\{\Delta F\}$ the maximum and minimum of ΔF across the sub-sampled distributions, respectively. As
470    $R_{\Delta \mathrm{F}}$ is susceptible to outliers, we further characterize the width of a distribution by the inter-quartile range, which is defined as the difference between the 75$^{\mathrm{th}}$ ($Q_{75\%}$) and 25$^{\mathrm{th}}$ ($Q_{25\%}$) percentiles of ΔF:

$$Q_{\Delta \mathrm{F}} = Q_{75\%}(\Delta F) - Q_{25\%}(\Delta F) \tag{21}$$

Variations in θ are caused by the diurnal and seasonal cycle of the Earth, or variations along the longitude at a given time. Figure 5a shows distributions of solar ΔF_{sol} for $\theta = 0°$, ranging from -944.5 W m^{-2} (high IWC) to 78.0 W m^{-2} (high α_{srf}).
475   For simulated $\theta < 85°$, the median values range from -11.9 to -12.9 W m^{-2} with an intensification of ΔF_{sol} towards larger θ. At the same time, the upper maxima of ΔF_{sol} are shifted towards zero, which is a combination of three effects: i) a decreasing downward irradiance at TOA with increasing θ; ii) an increasing optical path length s through the cloud with increasing θ and the corresponding increase in scattering; and iii) an increase in upward scattered radiation with increasing θ as the light rays get slanted and a larger fraction of radiation from the forward scattering range is directed upwards. Effects i) and ii) compete
480   and are dominated by effect iii). The combination of effects i) to iii) also reduces the inter-quantile for larger θ and indicates a reduced influence of the other free parameters on ΔF_{sol}. However, the smallest ΔF_{sol} is calculated for θ of 85° and is caused by the reduced side-ward scattering of ice crystals.

The value of θ where ΔF_{sol} is most intense depends on α_{srf} and is typically located between 50° and 70° (Markowicz and Witek, 2011). The maximum in ΔF_{sol} and the corresponding θ are explained by the strong forward scattering peak of ice
485   crystals and the resulting weak backscattering (Haywood and Shine, 1997; Myhre and Stordal, 2001). To further elaborate on the response of ΔF_{sol} on large θ, Fig. 6a shows ΔF_{sol} as a function of θ for selected τ_{ice} and α_{srf}. For an optically thick cirrus with $\tau_{\mathrm{ice}} = 6.62$ located over a surface with $\alpha_{\mathrm{srf}} = 0$ (blue, solid curve) the maximum ΔF_{sol} appears around $\theta = 50°$. For
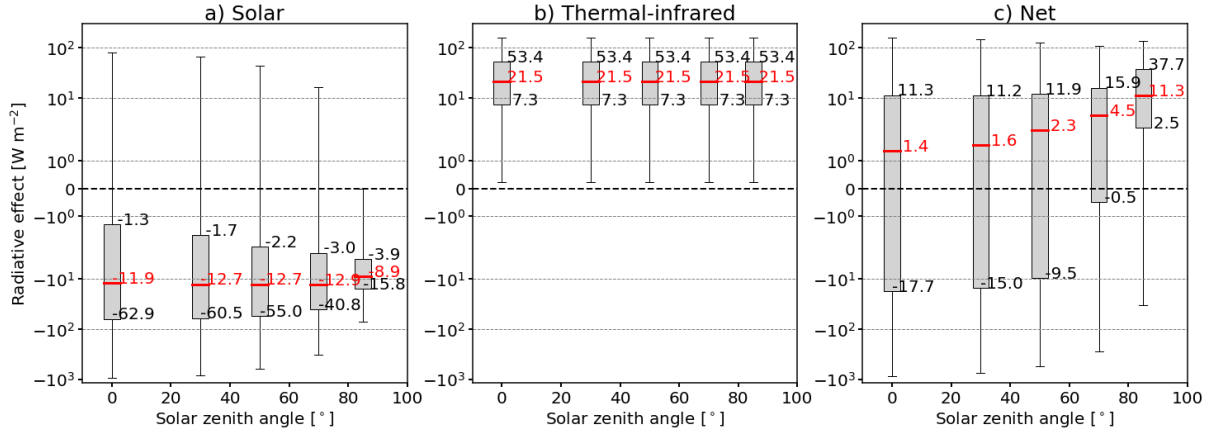
Figure 5. Box plots of **(a)** solar, **(b)** TIR, and **(c)** net ΔF (in W m^{-2}) as a function of the solar zenith angle θ. Median values are indicated in red, the 25 % – 75 % range is represented by the gray boxes, and the 10 % and 90 %-percentiles are given by the whiskers. Red and black numbers indicate the 25$^{\text{th}}$- and 75$^{\text{th}}$ percentiles, and the median value, respectively. Note the logarithmic scale on the y-axis.
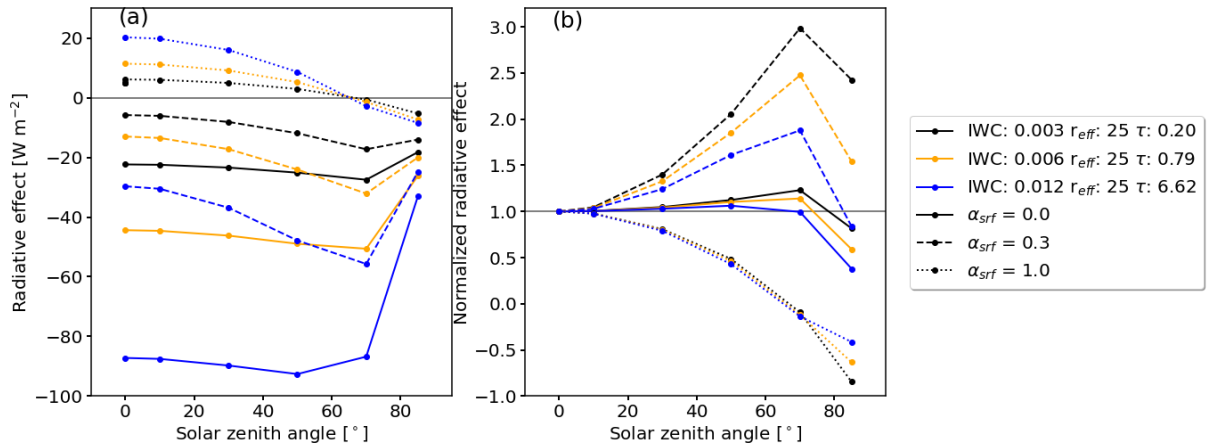
Figure 6. (a) Solar radiative effect ΔF_{sol} (in W m^{-2}) as function of solar zenith angle θ for three ice clouds with cloud optical thickness τ_{ice} of 0.1, 0.4, and 1.6. Effective radius r_{eff} is given in units of μm and the ice water content IWC in units of g m^{-3}. The cloud is located over surfaces with a surface albedo α_{srf} of 0, 0.3, and 1. **(b)** Same as **(a)** but normalized with ΔF_{sol} of each case at $\theta = 0°$.
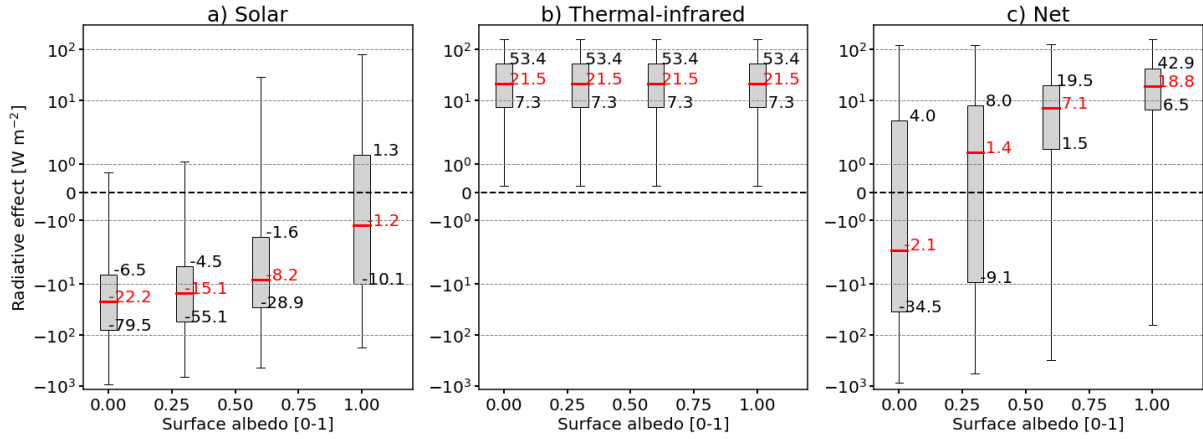
Figure 7. Same as Fig. 5 but as a function of the surface albedo α_{srf}.

the same cloud above a more reflective surface with $\alpha_{\mathrm{srf}} = 0.3$ (blue, dashed curve) the maximum is shifted towards $\theta = 70°$. Further increasing α_{srf} to 1 (blue, dotted curve), solar cooling turns into a heating and the strongest solar cooling is found for the largest θ. Figure 6a also shows that the shift in absolute, maximum ΔF_{sol} is most pronounced for optically thicker clouds. However, the largest relative change in ΔF_{sol} by varying θ appears for optically thin clouds (Coakley and Chylek, 1975).

Figure 6b shows ΔF_{sol} normalized with the respective ΔF_{sol} at $\theta = 0°$. The sensitivity of normalized ΔF_{sol} on θ is most pronounced for optically thin clouds with $\tau_{\mathrm{ice}} = 0.2$ over a moderately reflective surface ($\alpha_{\mathrm{srf}} = 0.3$) (dashed, black). For this combination, ΔF_{sol} at $\theta = 70°$ is a factor of 3 larger compared to a Sun overhead ($\theta = 0°$). The same cloud over a non-reflective surface ($\alpha_{\mathrm{srf}} = 0$) reduces the sensitivity leading to a factor of 1.2 in relation to ΔF_{sol} at $\theta = 0°$ (solid, black). A similar pattern but with a generally reduced sensitivity is found for the optically thicker cloud case with $\tau_{\mathrm{ice}} = 6.62$. In this case ΔF_{sol} is larger by a factor of 1.05 at $\theta = 50°$ (blue, solid) and larger by a factor of 1.7 at $\theta = 70°$ (blue dashed) with respect to a Sun at $\theta = 0°$. The large sensitivity for optically thin clouds is explained by the dominance of single-scattering, where scattering is strongly dependent on the value of the $\mathcal{P}$ at a given scattering angle. When the cloud becomes optically thicker, multiple-scattering processes start to dominate the RT and $\mathcal{P}$ is averaged over a range of scattering angles, reducing the sensitivity on θ. However, while the sensitivity might be largest for optically thin clouds, the absolute ΔF_{sol} of optically thin clouds is small compared to clouds with higher τ_{ice}.

Figure 5b shows that ΔF_{tir} is unaffected by θ leading to a constant median ΔF_{tir} of 21.5 W m^{-2}. The highest positive values of ΔF_{tir} (strongest warming effect) are found for clouds with maximal IWC. The resulting ΔF_{net}, shown in Fig. 5c, is dominated by a warming in the TIR that leads to median ΔF_{net} between 1.4 W m^{-2} and 11.3 W m^{-2}, with a minimum of ΔF_{net} of -872.8 W m^{-2} and maximum of 160.1 W m^{-2}. With increasing θ, ΔF_{net} increases. This is caused by the shift of the lower minima of ΔF_{sol} towards zero, which indicates that a larger fraction of the simulations have a reduced solar cooling effect and, thus, the fraction of simulations with a positive ΔF_{net} (net warming) increase. The reduced variability of ΔF_{sol} with increasing θ propagates into the distribution and variability in ΔF_{net}.
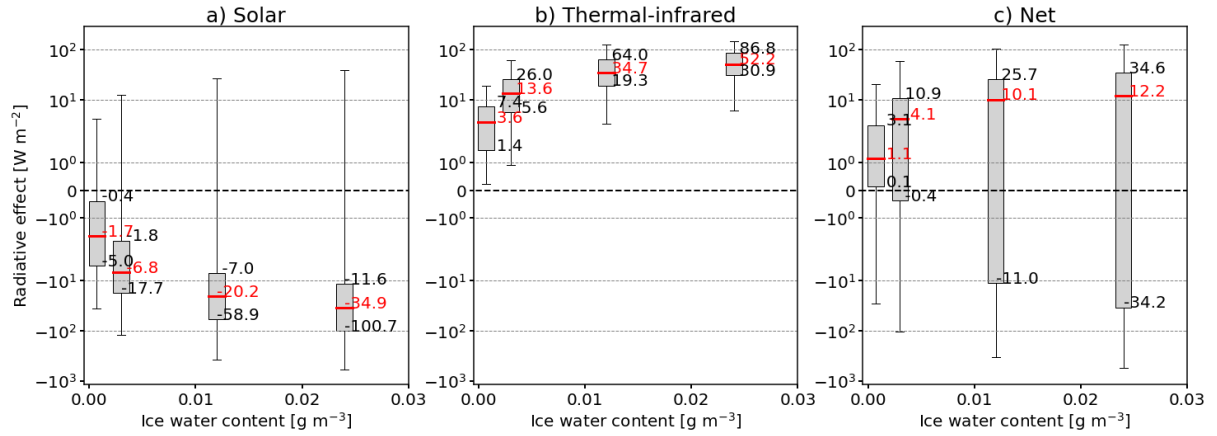
Figure 8. Same as Fig. 5 but as a function of ice water content IWC (in $\mathrm{g\,m^{-3}}$). For better legibility only IWC up to 0.03 $\mathrm{g\,m^{-3}}$ are plotted.

510   The influence of the underlying surface is shown in Fig. 7. For $\alpha_{\mathrm{srf}} = 0$ the surface absorbs the entire incident solar radiation creating the largest contrast between α_{srf} and the cloud albedo α_{cld}. When the surface is fully absorbing ($\alpha_{\mathrm{srf}} = 0$), almost all simulated cloud combinations are characterized by a cooling in the solar with ΔF_{sol} ranging from -944.5 to $80\ \mathrm{W\,m^{-2}}$. The cooling is reduced when the surface becomes more reflective and the contrast between surface and cloud is reduced, which shifts the distributions and their medians towards positive ΔF_{sol}. With α_{srf} approaching 0.66, around 25 % of the

515   parameter combinations lead to a solar heating. This becomes even more pronounced towards $\alpha_{\mathrm{srf}} = 1$, where around 50 % of the simulations yield a warming effect in the solar. ΔF_{tir} is unaffected by changes in α_{srf}, as expected, and remains constant for all α_{srf} with a median at 21.5 $\mathrm{W\,m^{-2}}$. The resulting ΔF_{net} is dominated by a net warming effect, indicated by mostly positive median values ranging from 1.4 $\mathrm{W\,m^{-2}}$ ($\alpha_{\mathrm{srf}} = 0.25$) to 18.8 $\mathrm{W\,m^{-2}}$ ($\alpha_{\mathrm{srf}} = 1$). An exception is $\alpha_{\mathrm{srf}} = 0$, where more than 50 % of the simulations lead to a net cooling with a median ΔF_{net} at $-2.1\ \mathrm{W\,m^{-2}}$.

520   **3.3   Sensitivity on ice water content and ice crystal radius**

As presented in Fig. 2, the IWC is the second most influencing factor that controls ΔF. For a constant crystal number concentration the increase in IWC leads to an increase in r_{eff}, as well as the total particle scattering and absorption cross-sections. This enhances scattering and absorption along the optical path s though the cloud. Figure 8a reveals that with increasing IWC the median of ΔF_{sol} becomes more negative (intensification of the cooling effect in the solar part of the spectrum). The steepest

525   increase is found for IWC $< 0.012\ \mathrm{g\,m^{-3}}$, while for IWC $\geq 0.012\ \mathrm{g\,m^{-3}}$ the solar cloud RE saturates. At the same time $Q_{\Delta F,\mathrm{sol}}$, given by Eq. 21, increases, indicating an enhanced sensitivity of ΔF_{sol} on the free parameters. The minimum and maximum of ΔF_{sol} result from clouds over highly reflective surface ($\alpha_{\mathrm{srf}} = 1$) and clouds containing crystals with the smallest $r_{\mathrm{eff}} = 5\ \mu\mathrm{m}$.

For ΔF_{tir} the increase in IWC leads to an intensified warming effect (Fig. 8b). Again, this is caused by the increase in the total particle scattering and absorption cross-sections. Similarly to ΔF_{sol}, the steepest increase in ΔF_{tir} appears for

530   IWC $< 0.012\ \mathrm{g\,m^{-3}}$, while for larger IWC the medians approach an almost constant level and a further increase in IWC has
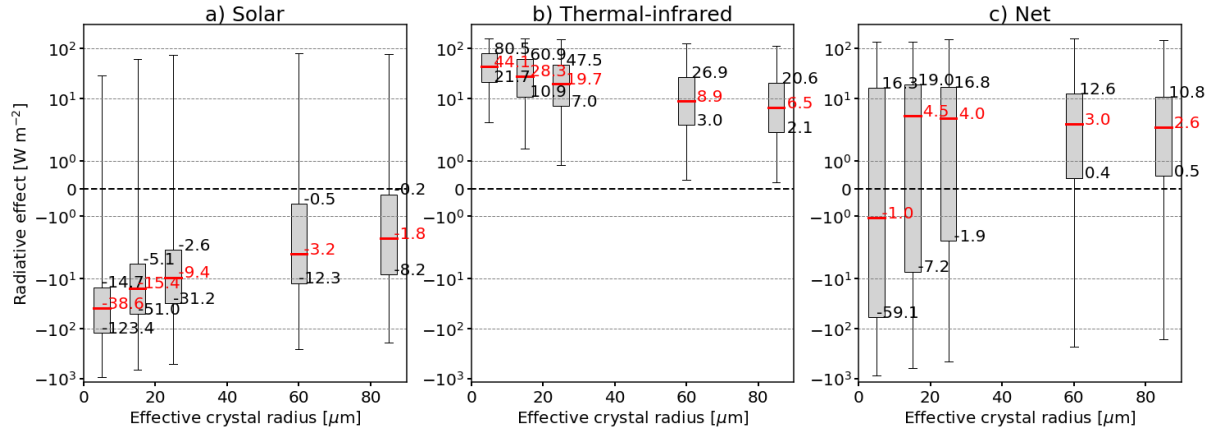
Figure 9. Same as Fig. 5 but as a function of effective crystal radius r_{eff} (in μm).

only a limited effect on ΔF_{tir}. The resulting ΔF_{net} (Fig. 8c) ranges from -543.2 to 125.5 W m^{-2} and is skewed to positive ΔF_{net} with median values between 1.1 and 12.2 W m^{-2}.

The size of ice crystals also influence the cloud RE, with a larger sensitivity of ΔF_{sol} on r_{eff} than ΔF_{tir} (Baum et al., 2005b). Figure 9a illustrates that cirrus with the smallest r_{eff} are associated with the most intense cooling effect in the solar,

535   leading to ΔF_{sol} between -944.5 and 80.0 W m^{-2}. Small crystals and high number concentrations lead to higher $\alpha_{\text{cld,ice}}$ in the solar compared to fewer and larger crystals (Stephens et al., 1990; Zhang et al., 1994). For the smallest crystals in the simulations a median ΔF_{sol} of -38.6 W m^{-2} is determined. For increasing r_{eff} the cooling effect in the solar range decreases and tends towards ΔF_{sol} of -1.8 W m^{-2}. The intensified solar cooling (more negative ΔF_{sol}) with decreasing r_{eff} is associated with an increase in the ice crystal number concentration, while keeping IWC constant, which is also known as

540   cloud albedo effect. In addition, ice crystals with larger r_{eff} are characterized by enhanced forward scattering. Hence, less radiation is scattered to the sides or backwards into space. Figure 9a shows that clouds with larger r_{eff} are less sensitive to the effect of the free parameters as the inter-quartile range decreases strongly from $Q_{\Delta F,\text{sol}}(r_{\text{eff}} = 5\,\mu\text{m}) = 108.7$ W m^{-2} to $Q_{\Delta F,\text{sol}}(r_{\text{eff}} = 85\,\mu\text{m}) = 8.0$ W m^{-2}. Similarly, Fig. 9b shows the strongest TIR heating for the smallest crystals / highest N_{ice}. Such clouds have the largest total absorption cross-section and act almost as blackbodies in the TIR (Stephens et al., 1990;

545   Zhang et al., 1994). However, an increase in r_{eff} while fixing IWC leads to a reduction in ΔF_{tir}, which is caused by the lower total particle scattering and absorption cross-sections. $Q_{\Delta F,\text{tir}}$ decreases from 58.8 W m^{-2} for $r_{\text{eff}} = 5\,\mu$m to 18.5 W m^{-2} for $r_{\text{eff}} = 85\,\mu$m. Median values of ΔF_{net}, shown in Fig. 9c indicate only a net cooling for $r_{\text{eff}} = 5\,\mu$m with -1 W m^{-2}, whereby elsewhere a net warming is dominant with ΔF_{net} between 2.6 and 4.5 W m^{-2}. Simultaneously, $Q_{\Delta F,\text{net}}$ slightly decreases, which indicates the reduced impact of the remaining free parameters for large crystals. The presented dependencies, especially

550   for small r_{eff}, of solar, TIR, and net ΔF on r_{eff} and IWC agree with previous studies, e.g., from Hansen and Travis (1974), but particularly Fu and Liou (1993) and Zhang et al. (1999).

3.4 Multi-dimensional dependencies on θ, α_{srf}, r_{eff}, and IWC
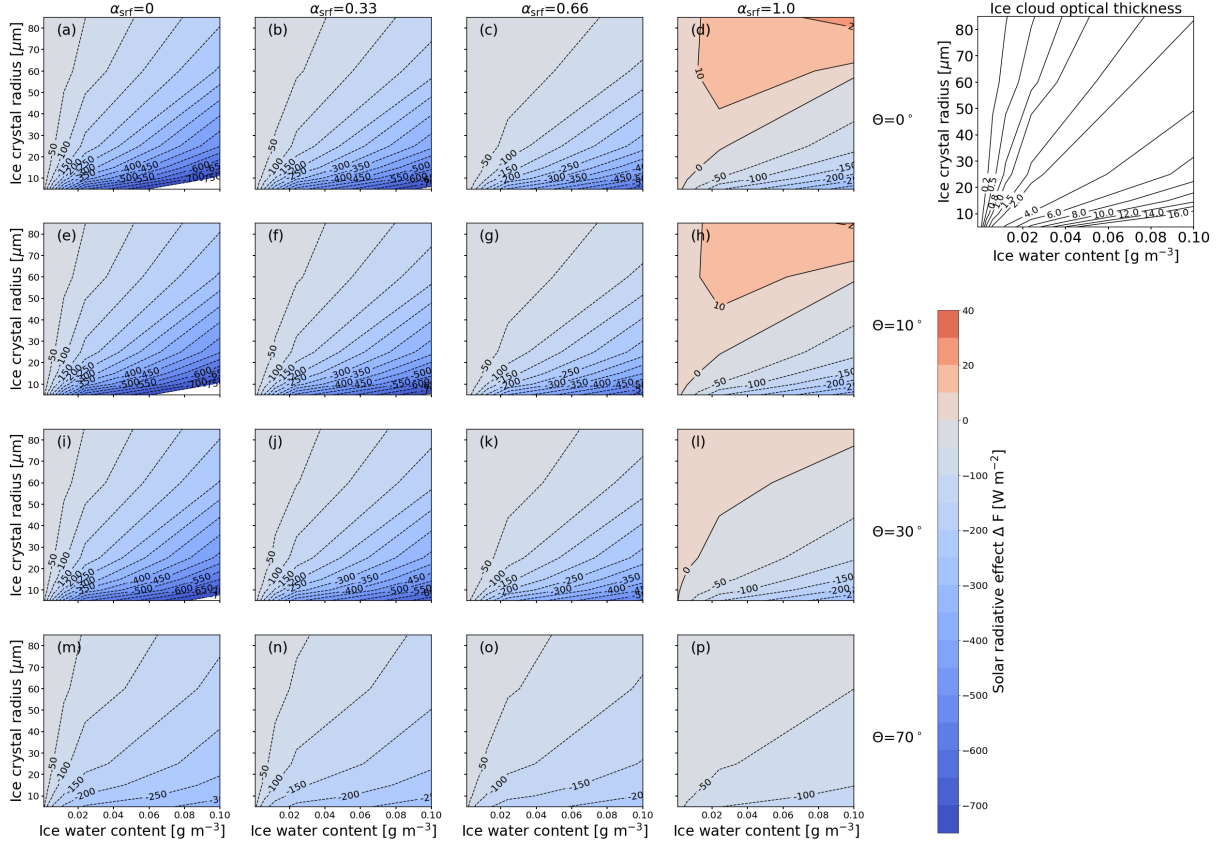
Figure 10. Solar cloud radiative effect ΔF_{sol} in $\mathrm{W\,m^{-2}}$ sampled into two-dimensional parameter space of ice water content IWC (in $\mathrm{g\,m^{-3}}$) and effective radius r_{eff} (in $\mu\mathrm{m}$). Each panel represents combinations of surface albedo α_{srf} and solar zenith angle θ. Blue values indicate negative ΔF_{sol} (cooling) and red values indicate positive ΔF_{sol} (warming). The contour lines provide a direct measure of the sensitivity to the indicated parameters. The top-right panel shows, for reference, the cloud optical depth τ at 550 nm wavelength that corresponds to the combinations of r_{eff} and IWC shown on the other panels.

The previous analysis aimed to sample the 8D-hypercube in a series of 1D–cross-sections to focus on the general distribution of ΔF that result from a single parameter. This likely masks dependencies of ΔF on specific parameter combinations that are closely interconnected. Subsequently, we focus on a detailed analysis, particularly in the solar wavelength range, to highlight the dependencies among Sun geometry, surface albedo, and cloud properties - especially r_{eff} and IWC.

3.4.1 Solar radiative effect

Figure 10 shows ΔF_{sol} as a function of IWC and r_{eff} for combinations of α_{srf} (columns) and θ (rows). Moving from the left to the right column the surface becomes more reflective (increasing α_{srf}) and going from the top to the bottom row the Sun approaches the horizon (increasing θ).

Figure 10a represents non-reflective surfaces and a Sun at the zenith. In these cases and focusing on ice crystals with $r_{\text{eff}} > 30\,\mu$m the contour lines are well separated. A wide spacing of the contour lines indicates a low sensitivity of ΔF_{sol} on IWC and r_{eff}. In those regions ΔF_{sol} ranges from 0 to -450 W m^{-2} (cooling), with an intensification of ΔF_{sol} for decreasing r_{eff}. The contour lines get closer for $r_{\text{eff}} < 30\,\mu$m and align with the x-axis, which indicates an increase in the sensitivity of ΔF_{sol}, particularly with respect to r_{eff}, as it is expected from Fig. 2.

For the Sun at zenith and cirrus above reflective surfaces ($0 < \alpha_{\text{srf}} < 1$), the sensitivity with respect to IWC and r_{eff} is generally reduced. This results from the increasing contribution of surface reflected, upward irradiance, which progressively dominates ΔF_{sol} of the cirrus. ΔF_{sol} is essentially a measure of the contrast between α_{srf} and $\alpha_{\text{cld,ice}}$, with $\alpha_{\text{cld,ice}}$ mostly dependent on r_{eff} and IWC. In case of a highly reflective surface ($\alpha_{\text{srf}} \geq 0.6$; Fig. 10d) the predominant cooling in the solar spectrum turns into a warming effect for most of the combinations with ΔF_{sol} up to 15–20 W m^{-2}. Only ice clouds with $r_{\text{eff}} < 20$–30 μm and IWC $\approx$ 0.04–0.1 g m^{-3}, i.e., high $\tau_{\text{ice}} > 3$, are more reflective than the surface. Such combinations of $r_{\text{eff}} < 20\,\mu$m and IWC $\approx$ 0.04–0.1 g m^{-3} are associated with ice crystal number concentrations that are rarely observed in nature except for some cases of young contrails (see Fig. 1 in Krämer et al. (2016)).

For cirrus over non-reflective or slightly reflective surfaces ($\alpha_{\text{srf}} \leq 0.33$) and the Sun at intermediate SZA ($\theta \geq 30°$), the contour lines separate and the sensitivity of ΔF_{sol} on r_{eff} and IWC is reduced. However, this effect is less pronounced compared than a change in α_{srf}. For Sun positions closest to the horizon ($\theta = 70°$) and above highly reflective surfaces ($\alpha_{\text{srf}} = 1$), ΔF_{sol} in Fig. 10p is characterized by a generally low sensitivity over the entire range of IWC and r_{eff}. In spite of the warming effect for $\alpha_{\text{srf}} = 1$ and $\theta \leq 30°$, the slant optical path of the incident radiation through the cloud reduces the surface influence and leads to a cooling effect with ΔF_{sol} in the range of -5 to -100 W m^{-2}.

3.4.2 Thermal-infrared and net radiative effect

The TIR component of ΔF is insensitive to changes in θ and α_{srf}, and only combinations of IWC and r_{eff} are of relevance. In the TIR, the surface is approximated by a blackbody with a wavelength independent emissivity equal to one. The resulting distributions of ΔF_{net}, shown in Fig. 11, are dominated by the contribution of ΔF_{sol} and, therefore, are characterized by similar sensitivities. The strongest gradient of ΔF_{net} on IWC and r_{eff} are found for $\theta \approx 0°$ and $\alpha_{\text{srf}} = 0$ (Fig. 11a). With increasing α_{srf}, ΔF_{net} becomes positive for the majority of the combinations of IWC and r_{eff} (Fig. 11d) with the net warming being most pronounced for $\alpha_{\text{srf}} = 1$, (Fig. 11d). It is further noted that for $\alpha_{\text{srf}} = 1$, $\theta \leq 30°$, and $\tau_{\text{liq}} < 1$, ΔF_{net} is positive and almost exclusively sensitive to IWC, while for $\alpha_{\text{srf}} = 1$, $\theta \leq 30°$, and $\tau_{\text{liq}} > 1$, ΔF_{net} also becomes sensitive to r_{eff}. In addition, regions that have a net cooling effect, i.e., at high N_{ice} values, are exclusively sensitive to r_{eff}. The cloud can have a net cooling effect, when the Sun is close to horizon (Fig. 11p), with almost no sensitivity to r_{eff} and IWC.
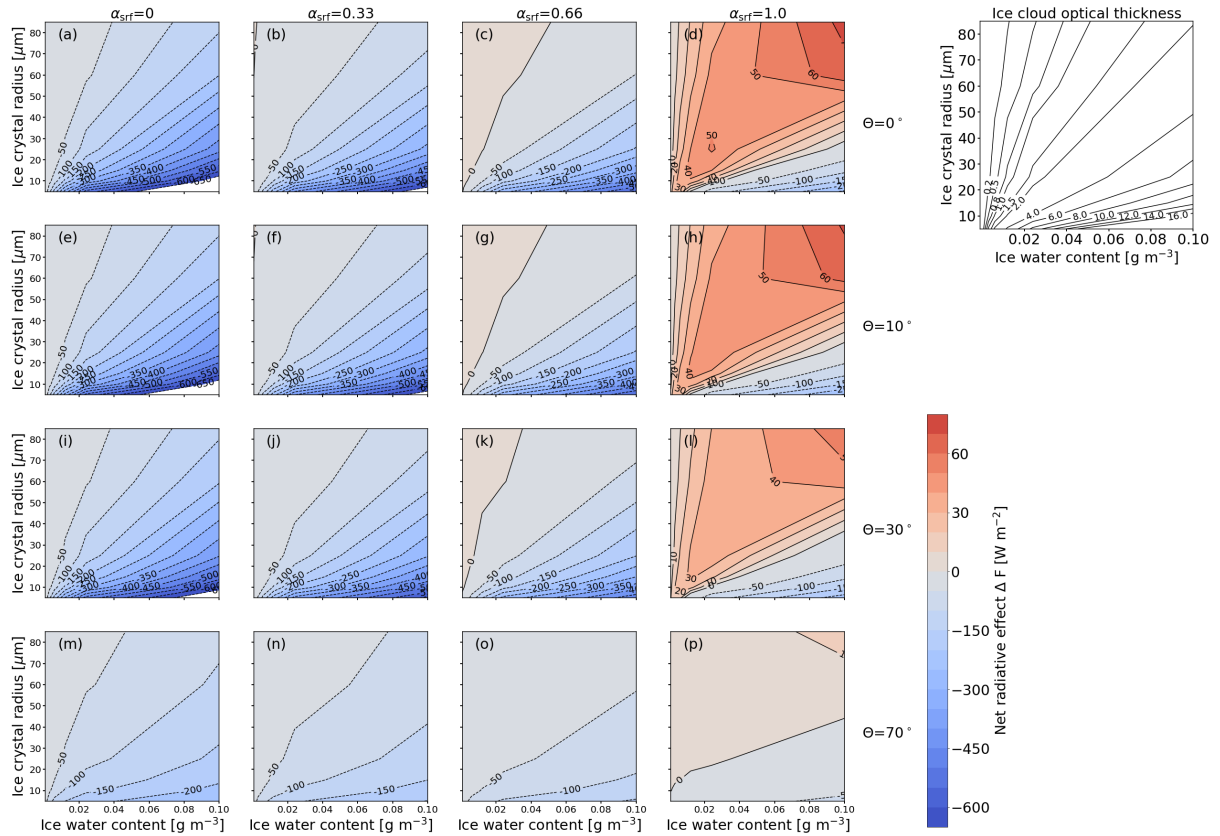
Figure 11. Same as Fig. 10 but for ΔF_{net} (in $\mathrm{W\,m^{-2}}$).

3.5 Sensitivity on atmospheric profile, surface temperature, relative humidity, ice cloud altitude, and ice cloud geometric thickness

Within this study, the atmospheric profiles, the surface temperatures T_{srf}, as well as the vertical location of the ice cloud are coupled. For example, the selection of the US standard atmosphere is directly linked to a surface temperature of $T_{\mathrm{srf}} = 288.2$ K. T_{srf} is equal to the lowermost temperature value in the respective AP. The vertical position of the ice cloud depends on the temperature of the AP and the selected cloud top temperature $T_{\mathrm{cld,ice}}$ (see Appendix B and Fig. B1a,b therein).

Figure 12a shows that variations in T_{srf} have an effect on ΔF_{sol} with differences in median ΔF_{sol} of up to $\pm 7\ \mathrm{W\,m^{-2}}$. Generally larger effects are found for the TIR component, where an increase in T_{srf} enhances the temperature difference between surface and cirrus, which leads to an intensification of the TIR heating (see Eq. 19 and Corti and Peter (2009)), shifting the median ΔF_{tir} from 3.6 to 13.6 $\mathrm{W\,m^{-2}}$ (Fig. 12b). Simultaneously, the distributions broaden with increasing T_{srf} with $Q_{\Delta F,\mathrm{tir}}$ ranging from 1.4 to 7.4 $\mathrm{W\,m^{-2}}$ (257.2 K) and 5.6 to 26.0 $\mathrm{W\,m^{-2}}$ (299.7 K), which results from the warmer and moister tropical profile compared to the drier Subarctic profile. As a result of the almost constant ΔF_{sol} and the increase in ΔF_{tir}, the net heating effect is enhanced with medians ranging between 0.7 and 6.6 $\mathrm{W\,m^{-2}}$.
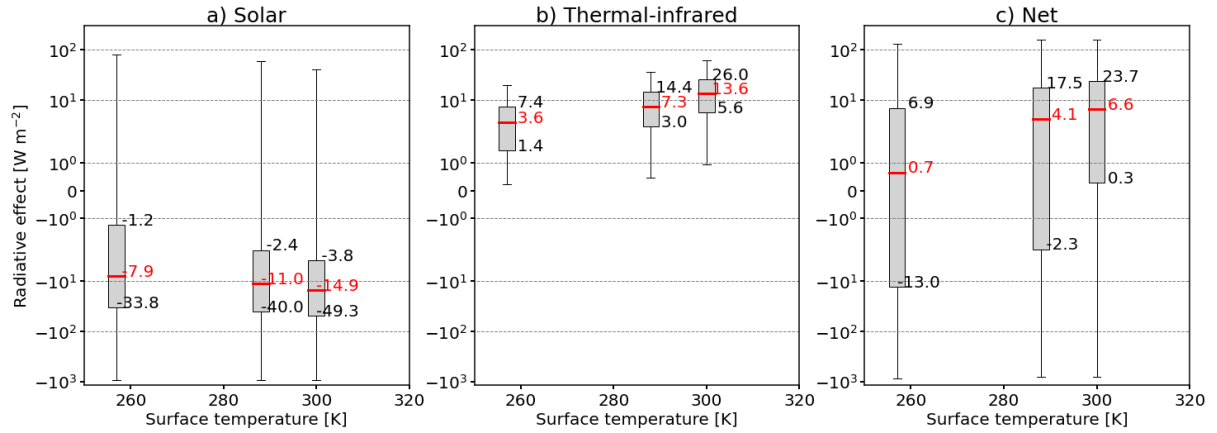
Figure 12. Same as Fig. 5 but for surface temperature T_{srf} (in K).
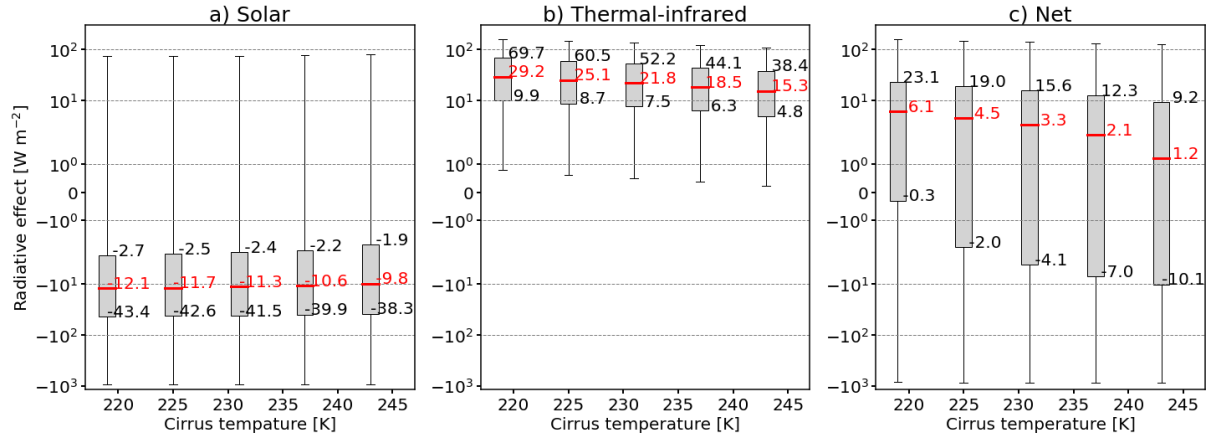
Figure 13. Same as Fig. 5 but for ice cloud temperature $T_{\mathrm{cld,ice}}$ (in K).

The effect of variations in $T_{\mathrm{cld,ice}}$ are shown in Fig. 13a–c. Increasing $T_{\mathrm{cld,ice}}$ reduces the temperature difference between surface and ice cloud, and therefore the TIR heating effect (Fig. 13b). Median ΔF_{tir} are reduced from 29.2 to 15.3 W m^{-2},

605   when $T_{\mathrm{cld,ice}}$ is increased from 219 to 243 K. Compared to the impact of T_{srf}, which was varied over a range of 42.5 K, shifting the cloud in the vertical has only a minor effect on ΔF_{tir} and ΔF_{net}, as the variation in $T_{\mathrm{cld,ice}}$ spanned only 24 K. The resulting net effect from variations in $T_{\mathrm{cld,ice}}$ leads to medians between 1.2 and 6.1 W m^{-2} for $T_{\mathrm{cld,ice}}$ of 219 and 243 K, respectively.

    The previously mentioned impact of T_{srf} on ΔF_{sol} is traced back to: a) the different optical path length through the at-

610   mosphere because of variations in cloud top altitude; and b) the different water vapor concentration due to the three applied APs. The effect of varying RH profiles were investigated by manipulating the original RH profiles by $\pm 20\,\%$ representing the variability in RH reported by Anderson et al. (1986). The RT simulations were performed for a sub-set of the parameter space
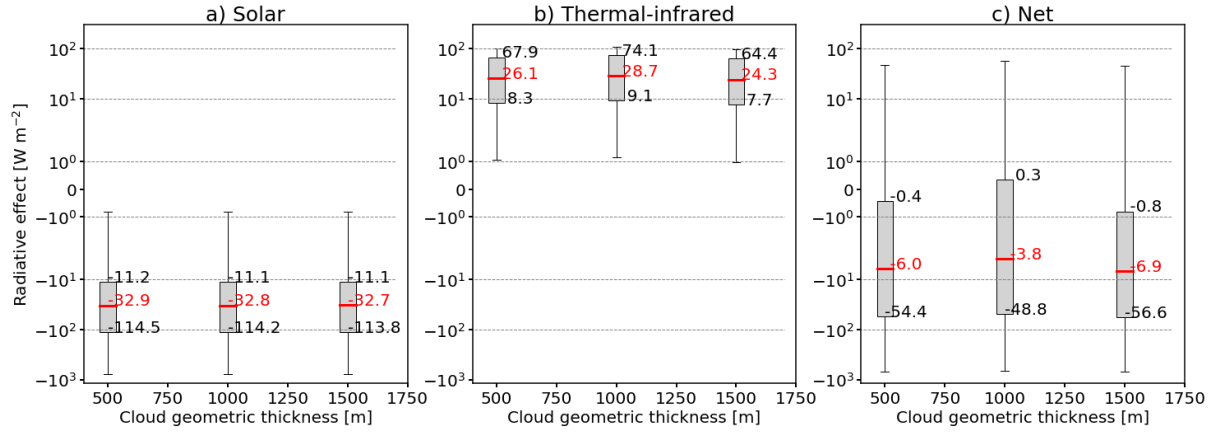
Figure 14. Same as Fig. 5 but for the cloud geometrical thickness dz (in m) and only for a sub sample of the parameter space. Values for ice cloud temperature T_{ice} = 231 K, surface temperature T_{srf} = 288.2 K, surface albedo α_{srf} = 0.15, and liquid water cloud optical thickness τ_{liq} = 0. Values for solar zenith angle θ, ice water content IWC, and effective radius r_{eff} are varied.

with fixed $T_{cld,ice}$ = 231 K, α_{srf} = 0, and τ_{liq} = 0. The effects on solar, TIR, and net ΔF are quantified by their absolute and relative differences. Variations in RH have only a small effect on ΔF_{sol} with maximal ± 0.15 W m^{-2} (± 0.4 %) among all profiles. A slightly larger impact is found for ΔF_{tir} with up to ± 1.45 W m^{-2} (± 4.1 %) in case of the warm and moist tropical profile (`afglt`). Less affected are the standard atmosphere (`afglus`), where ΔF_{tir} varies by ± 0.9 W m^{-2} (± 3.2 %) and the dry Subarctic profile (`afglsw`) with variations in ΔF_{tir} of ± 0.3 W m^{-2} (± 2.4 %). Consequently, `afglt` has the largest variation in ΔF_{net} of ± 0.8 W m^{-2} (± 8 %) and is followed by ± 0.6 W m^{-2} (± 3.8 %) for `afglus` and ± 0.2 W m^{-2} (± 0.6 %) for `afglsw`. Scaling the original RH profiles showed that variations on the RH profile explicitly influence the TIR wavelength range but particularly the net RE. This analysis suggests that the variations in RH have to be considered as potential source of variability, when using this publicly available data set.

All simulations within this study were performed for a fixed cloud geometric thickness dz of 1000 m. In reality however, dz is likely to vary over the cirrus lifetime, for example due to sedimentation of ice crystals or vertical winds. The effect of changing dz is quantified by a dedicated sensitivity analysis of ΔF for a sub-sample of the full parameter range (Table 4). A similar sub-parameter space is used as for the RH sensitivity but additionally fixing T_{srf} = 288 K, i.e., using the `afglus` profile. With τ_{ice} being proportional to the IWP of the cloud (Eq. 10), the IWP of the 1000 m reference and solar τ_{ice} are kept constant, and the IWC for the clouds with dz of 500 and 1500 m clouds is scaled accordingly.

As expected from Eq. 10, the resulting effect on median ΔF_{sol}, given in Fig. 14, is almost negligible with ± 0.1 W m^{-2} (± 0.3 %). Differences in median ΔF_{tir} are up to ± 0.6 W m^{-2} (± 3.5 %), which leads to differences in median ΔF_{net} of ± 0.6 W m^{-2} (± 6.2 %). The relevant relative differences in ΔF_{tir} and ΔF_{net} are explained by the varying cloud base altitude, which modifies the vertical distribution of IWC and the temperature of the cloud base, which determines the amount of emitted radiation. In addition, geometrically thin clouds with low τ_{ice} act as gray bodies, while with an increase in dz cirrus become
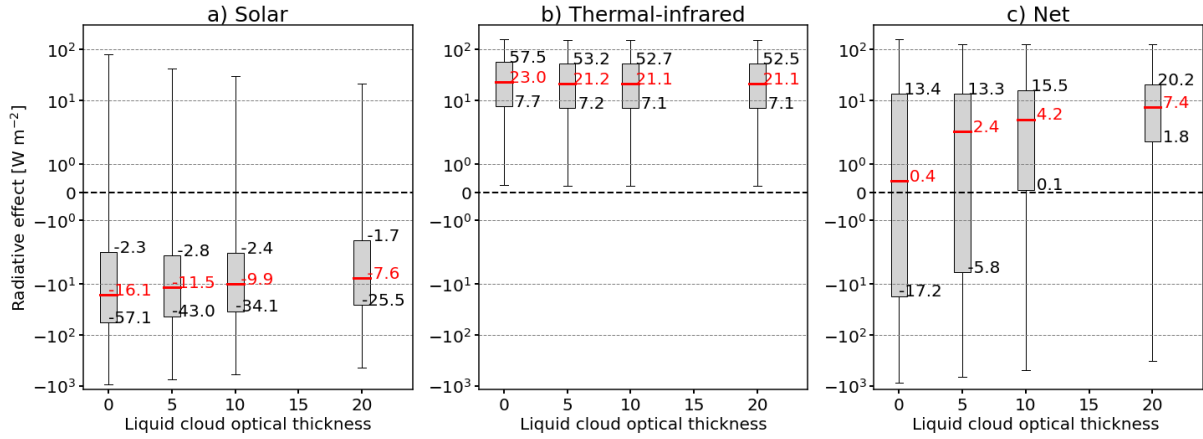
Figure 15. Same as Fig. 5 but for the underlying liquid water cloud optical thickness τ_{liq}.

opaque and act as more efficient black bodies (Corti and Peter, 2009). Fu and Liou (1993) further reported that cirrus with small r_{eff} reflect solar radiation at the cloud top (solar cooling) but absorb TIR radiation at the cloud base (TIR warming),

635 which creates a temperature gradient within the cloud that depends on dz. From the dz sensitivity analysis it is found that dz can be neglected in the solar wavelength range but is of relevance for ΔF_{tir} and especially ΔF_{net}, where absolute values are small. This partly agrees with the findings from Meerkötter et al. (1999) who showed that solar, TIR, and net ΔF are only slightly sensitive to changes in dz with solar, TIR, and net ΔF below 2 W m^{-2}, under the premise of a constant ice water path (IWP). The presented simulations indicate $\Delta\Delta F_{\mathrm{sol}}$ of 2 W m^{-2}, which is comparable to Meerkötter et al. (1999), but we found

640 slightly higher $\Delta\Delta F_{\mathrm{tir}}$ and $\Delta\Delta F_{\mathrm{net}}$ of 4.5 and 3.1 W m^{-2}, respectively.

3.6 Sensitivity on underlying liquid water cloud

The impact of an additional liquid water cloud on the cirrus ΔF is presented in Fig. 15. A liquid water cloud optical thickness $\tau_{\mathrm{liq}} = 0$ is equivalent to the absence of secondary clouds and such conditions lead to the strongest ΔF_{sol} with a median of -16.1 W m^{-2}. By gradually increasing τ_{liq} the reflected, upward irradiance overlays and masks the impact of the surface. In

645 general, the response of ΔF_{sol} on τ_{liq} is comparable to that of an increase in α_{srf}. Introducing a cloud with $\tau_{\mathrm{liq}} = 5$ slightly enhances the cooling in the solar spectrum ΔF_{sol} from -11.5 to -7.6 W m^{-2}. More notable is the reduction in the variability of ΔF_{sol} with the distribution becoming narrower and reducing $Q_{\Delta F,\mathrm{sol}}$ from 54.8 W m^{-2} to 23.8 W m^{-2}.

An increase in τ_{liq} from 0 to 5 shifts the median ΔF_{tir} from 21.1 to 23.0 W m^{-2}. With a further increase in τ_{liq} the medians remain almost constant, while the $Q_{\Delta F,\mathrm{tir}}$ slightly decreases. The reduction of maximum ΔF_{tir} is a consequence of

650 the attenuated temperature difference ΔT between the liquid water cloud and the ice cloud compared to the surface. The effect on ΔF_{tir} is small as the change in temperature from surface to liquid water cloud is small. In the case of the US standard atmosphere, where $\Delta T = 5$ K.
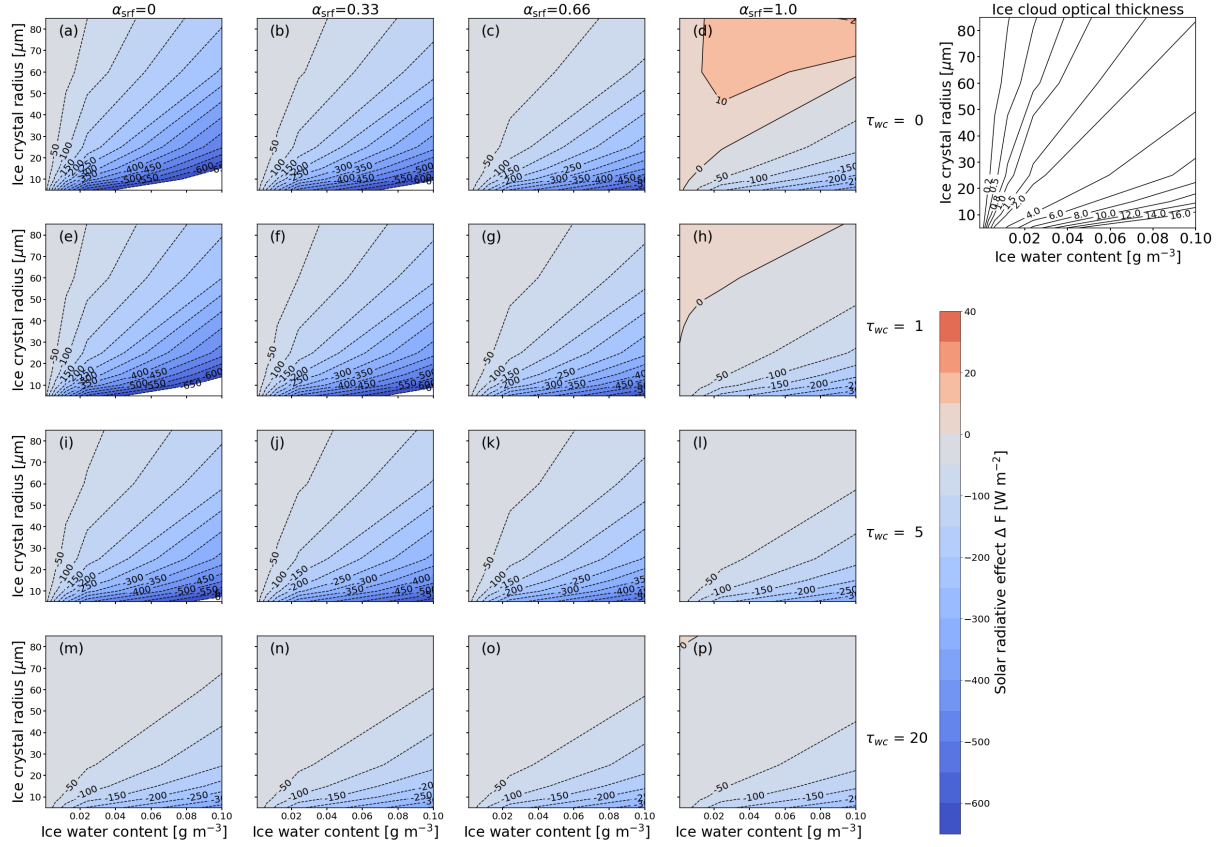
Figure 16. Same as Fig. 10 but ΔF_{sol} (in W m^{-2}) and combinations of surface albedo α_{srf} and cloud optical thickness τ_{liq} of the underlying liquid water cloud.

As a result of the reduced cooling in the solar spectrum and the stronger warming in the TIR spectrum, the net heating of the ice clouds intensifies with increasing τ_{liq}. The median ΔF_{net} is shifted from 0.4 to 7.4 W m^{-2} with an accompanying decrease in the overall variance. While for $\tau_{\text{liq}} < 5$ slightly fewer than 50 % of the combinations exert a potential net cooling by the cirrus, positive ΔF_{net} is dominating for larger τ_{liq}.

Figure 16 shows ΔF_{sol} depending on IWC and r_{eff} separated for α_{srf} (columns) and τ_{liq} (rows). In the presented cases, a θ of 10° is selected as the influence of the surface and an additional cloud layer is of higher importance, when the Sun is close to the zenith. Due to the selection of θ, the top row in Fig. 16 is the same as the second row in Fig. 10 with similar characteristic features in distribution and sensitivity: largest RE appears over dark surfaces ($\alpha_{\text{srf}} = 0$) in combination with clouds containing the largest ice number concentrations N_{ice} due to small r_{eff} and larger IWC. Increasing r_{eff} and / or reducing the IWC weakens ΔF_{sol}. Introducing the second cloud layer and gradually increasing τ_{liq} generally reduces the sensitivity on the ice cloud microphysical properties and the ice cloud RE. For the special case of $\alpha_{\text{srf}} = 1$, the introduction of a liquid water cloud turns
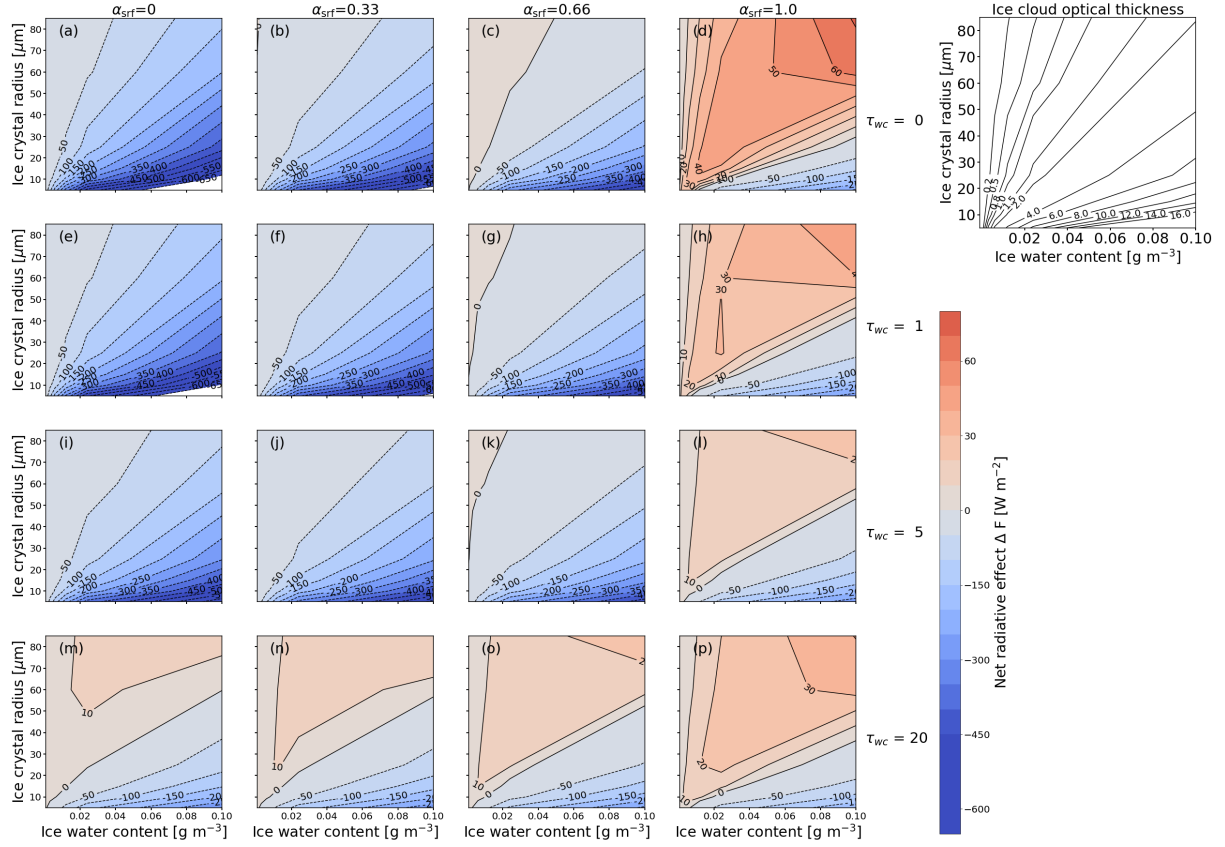
Figure 17. Same as Fig. 11 but for ΔF_{net} (in $\mathrm{W\,m^{-2}}$) and combinations of surface albedo α_{srf} and cloud optical thickness τ_{liq} of the underlying liquid water cloud.

the previous solar warming ($\Delta F_{\mathrm{sol}} \approx 10\ \mathrm{W\,m^{-2}}$) into a solar cooling effect of up to $\Delta F_{\mathrm{sol}} = -15\ \mathrm{W\,m^{-2}}$ for typical τ_{ice} of
665 contrails.

As shown in Fig. 15 the second cloud layer, at $z = 1500\ \mathrm{m}$ modifies ΔF_{tir} only slightly and multi-dimensional dependencies with respect to IWC, r_{eff}, α_{srf}, and τ_{liq} are weak leading to homogeneous distributions (not shown here). Figure 17 illustrates the variations in ΔF_{net}. For combinations of $\alpha_{\mathrm{srf}} \leq 0.66$ and $\tau_{\mathrm{ice}} \leq 5$, ΔF_{net} is determined by the solar component and its sensitivities. Special attention should be given to conditions with $\alpha_{\mathrm{srf}} \geq 0.66$ and $\tau_{\mathrm{ice}} > 0.8$, where ΔF_{net} turns from a cooling
670 into a warming effect. This is due to the reduced ΔF_{sol} and the domination by ΔF_{tir}. In these situations ΔF_{net} ranges between 0 and 60 $\mathrm{W\,m^{-2}}$. Increasing τ_{liq} leads to a reduction in the sensitivity of ΔF_{net} with respect to r_{eff} and IWC of the ice cloud. An exception are clouds with extreme N_{ice}, where an increased cooling effect in relation to r_{eff} occurs. Furthermore, cirrus over optically thick underlying clouds (last row) has a predominantly net warming effect.

4   Discussion

675 This study focused on the cloud RE of homogeneous, horizontally infinite ice cloud layers and neglected horizontal photon transport. The vertical and horizontal structure of ice clouds, i.e., distribution of ice water content, is typically heterogeneous, which is one reason for differences and uncertainties between 1D-simulated and the actual RE of such clouds (Fauchez et al., 2017, 2018). Additional differences originate from the independent pixel approximation (Cahalan et al., 1994).

For completeness and to raise awareness of potential uncertainties in the present simulations due to the effects of cloud 680 heterogeneity and 3D-scattering on the estimated RE, we provide a brief overview of the relevant literature. The majority of past cirrus and contrail studies that quantified the RE sensitivity were based on one-dimensional (1D) RT simulations (Strauss et al., 1997; Meerkötter et al., 1999; Fahey et al., 1999; Stuber et al., 2006). While aged and spread contrails might be approximated as thin plane-parallel layers within a homogeneous atmosphere (Minnis et al., 1999), younger contrails and cirrus are heterogeneous in their horizontal and vertical distribution of IWC. The first study that investigated 3D-radiative 685 effects was performed by Schulz (1998). This study was followed by Gounou and Hogan (2007) and Forster et al. (2012), who used 3D Monte Carlo simulations and found differences in contrail solar RE between 1D and 3D simulations ranging from 5 to 40 %. The largest deviations were found for extreme cases, e.g., large solar zenith angle (Sun close to the horizon). With the Sun illuminating the contrail or cirrus from the side, extinction and absorption within the cloud increases and scattering at cloud sides becomes more important compared to an illumination from above. Enhanced scattering at cloud sides also increases 690 the likelihood that photons get scattered back into space instead of being absorbed. Such effects are not captured by 1D RT simulations. Concerning the TIR wavelength range, Gounou and Hogan (2007) found that horizontal photons transport can increase contrail radiative effect by around 10 %, which has to be considered in the calculation of the contrail net radiative effect.

However, there is no systematic bias in solar, TIR, and net RE between 1D and 3D simulations and the deviations decrease 695 with increasing cloud homogeneity. More specifically, the differences between 1D and 3D simulations changes in magnitude and sign depending on the cloud heterogeneity and the solar illumination geometry. We employ 1D simulations as the total number of simulations performed within this study and the computational cost for full 3D RT simulation is unpractical. Therefore, we highlight that the provided data set can be used for situations that can be approximated by plane-parallel clouds and solar zenith angles smaller than 70°. Results should be used carefully by considering that 3D radiative effects introduce 700 uncertainties.

The eight selected parameters discussed in this study were found to be the most influential on the cirrus RE. The selection is further supported by earlier studies, e.g., Fu and Liou (1993), Zhang et al. (1999), Meerkötter et al. (1999), Yang et al. (2010), or Mitchell et al. (2011). However, not all potential factors that impact the cirrus RE can be considered in such a parametric study. Additional influences like aerosol layers, more complex surface albedo, or multiple overlapping cirrus and contrails 705 have not been investigated here and represent additional degrees of freedom. For example, previous studies found that aerosols have only a minor influence on contrail RE (Meerkötter et al., 1999) and Sanz-Morère et al. (2021) reported that the impact of overlap between contrails on their RE is negligible.

5 Summary

The net radiative effect ΔF (RE) of cirrus and contrails depends on multiple factors related to the microphysical and macro-physical cloud properties, the cloud optical properties, and radiative properties of the environment. The presented study aimed to separate the effect of eight selected parameters: solar zenith angle θ, ice water content IWC, ice crystal effective radius r_{eff}, cirrus temperature $T_{\mathrm{cld,ice}}$, surface albedo α_{srf}, surface temperature T_{srf}, liquid water cloud optical thickness τ_{liq} of an underlying cloud, and three ice crystal shapes on the cirrus RE. In total, 283,500 radiative transfer (RT) simulations have been performed with the libRadtran RT code by varying the 8 parameters within the ranges that are typically associated with natural cirrus and contrails. The RT simulations were performed with a 1D solver (plane-parallel clouds) and 3D scattering effects were not considered despite the fact they are known to become relevant for large solar zenith angles ($\theta > 70°$.) Specific cases or sub-samples were selected and discussed, while the entire set of results is made available as a NetCDF file (Wolf et al., 2023).

For the presented cases the cirrus RE was discussed separately for the solar ΔF_{sol} and thermal-infrared (TIR) ΔF_{tir} part of the spectrum, but also for the combined net RE. Comparing to a chosen reference with $\theta = 0°$, $T_{\mathrm{cld,ice}} = 219$ K, $\alpha_{\mathrm{srf}} = 0$, $T_{\mathrm{srf}} = 299.7$ K, IWC $= 0.024$ g m^{-3}, $r_{\mathrm{eff}} = 85$ μm, $\tau_{\mathrm{liq}} = 0$ (no liquid water cloud), and resulting $\tau_{\mathrm{ice}} = 0.46$ (at 550 nm) it was found that r_{eff} has the largest impact on solar, TIR, and net RE. The second most important parameter is the IWC, which impacts ΔF_{sol} and ΔF_{tir} equally. In the selected case, ΔF_{sol} and ΔF_{tir} have opposite signs, meaning that the IWC has a relatively small impact on ΔF_{net}. It has to be noted that the counter-balancing effect only appears during daytime, when $\Delta F_{\mathrm{sol}} \neq 0$ W m^{-2}. Whether r_{eff} or IWC is the most impactful parameter depends on the r_{eff} chosen as a reference. However, the dominance of r_{eff} and IWC over all other parameters remains. At night, ΔF_{net} equals ΔF_{tir} and the cirrus heats the Earth-atmosphere-system. After r_{eff} and IWC, the solar RE of cirrus is determined by θ, α_{srf}, τ_{liq}, and the ice crystal shape in descending priority. The RE in the TIR spectrum is dominated by T_{srf}, $T_{\mathrm{cld,ice}}$, τ_{liq}, and the ice crystal shape. The combined net RE is controlled by α_{srf}, θ, and T_{srf}, sorted in decreasing importance. The relevance of selected parameters can differ for other τ_{ice} and ambient condition.

The impact of individual parameters on the solar, TIR, and net RE was further investigated and quantified by sub-sampling the entire set of simulations by fixing one parameter at a time, while the remaining parameters were allowed to vary. This can be interpreted as a type of a sub-sampling, by averaging all unfixed values of RE, to project ΔF onto the one-dimensional space.

– Variations in θ have no influence on ΔF_{tir} but only on ΔF_{sol}. The majority of simulated ΔF_{sol} becomes more intense (stronger cooling) with increasing θ and reaches a maximum for θ between $50°$–$70°$. For further increasing θ the cooling effect in the solar declines. The exact location of maximum ΔF_{sol} is primarily dependent on α_{srf}. Increasing θ, the impact of the other free parameters and the resulting ΔF_{sol} are reduced. Consequently, the majority of the simulations with negative ΔF_{sol} are exceeded by positive ΔF_{tir}, which leads to a positive median ΔF_{net} (warming).

– The projection of ΔF_{net} for varying α_{srf} showed that cirrus primarily cools in the solar, except for highly reflective surfaces with α_{srf} approaching 1, e.g., over ice covered regions. Contrarily, ΔF_{tir} is mostly positive and unaffected by

the variations in α_{srf}. ΔF_{tir} determines the resulting ΔF_{net}, which leads to a net heating effect, when α_{srf} exceeds the critical range of 0.25–0.3.

– An increase in IWC intensifies the cooling in the solar and the heating in the TIR. As both effects compete against each other and ΔF_{tir} dominates ΔF_{sol}, the resulting net RE is a warming. An exception appears for largest IWC, where the median ΔF_{net} is negative. Simultaneously, the increase in IWC causes an enhanced impact of the free parameters and associated uncertainties.

– Clouds with similar IWC but larger r_{eff} are comprised of fewer ice crystals, which reduces the cloud reflectivity (cloud albedo effect). Over the entire range of r_{eff} the sub-sampled data set is characterized by a negative ΔF_{sol} that is most intense for the smallest crystals. Similarly, ΔF_{tir} is largest for small crystals and decreases for large crystals. While the solar and TIR ΔF become less intense with r_{eff}, the decrease is more pronounced for ΔF_{sol} such that cirrus primarily has a positive ΔF_{net}. An exception are clouds with the smallest r_{eff} and high IWC that occur only in contrails that just formed over non-reflective surfaces.

– The surface temperature T_{srf} and ice cloud temperature $T_{\mathrm{cld,ice}}$ only affect the TIR component of ΔF. Increasing the absolute difference between T_{srf} and $T_{\mathrm{cld,ice}}$ leads to an intensified TIR and resulting net heating effect.

– An underlying liquid water cloud with an increasing τ_{liq} leads to a reduction in solar ΔF_{sol}. Simultaneously, the TIR heating remains almost constant, reducing the negative ΔF_{net} (cooling) that is finally turned into positive ΔF_{net} (net warming) for the majority of simulated cases.

Data availability. The three data-sets with all simulated irradiances, the calculated cloud radiative effect, and the ice cloud optical thickness are given in separate NetCDF-files. Each file represents an individual ice crystal shape. The data is available on the zenodo platform as Wolf et al. (2023)

Appendix A: Overview over the multi-parameter dependencies

Figures A1 and A2 show solar ΔF_{sol} and TIR ΔF_{tir} (above diagonal), and net ΔF_{net} (below diagonal) for combinations of parameters indicated along the x- and y-axis. Both plots are intended to provide an overview over the multi-parameter dependencies. Within each sub-panel ΔF is given as a function of the x- and y-axis, while the other parameters are set to constant values that are representative of contrails and cirrus clouds. For example, the 'IWC–SZA' panel shows ΔF as a function of IWC, with $\theta = 30°$, $T_{\mathrm{cld,ice}}$ = 231 K, $r_{\mathrm{eff}} = 25$ μm, $\alpha = 0.15$, $T_{\mathrm{srf}} = 288$ K, and without a second liquid water cloud ($\tau_{\mathrm{liq}} = 0$). This can be understood as a 2D–cross-section of the 8D–hypercube. The black arrows indicate the gradient of the field. The gradient is computed with second order central differences and one-side differences at the boundaries of the field. The length of the arrow is only representative for an individual field and cannot be compared with the other fields as it
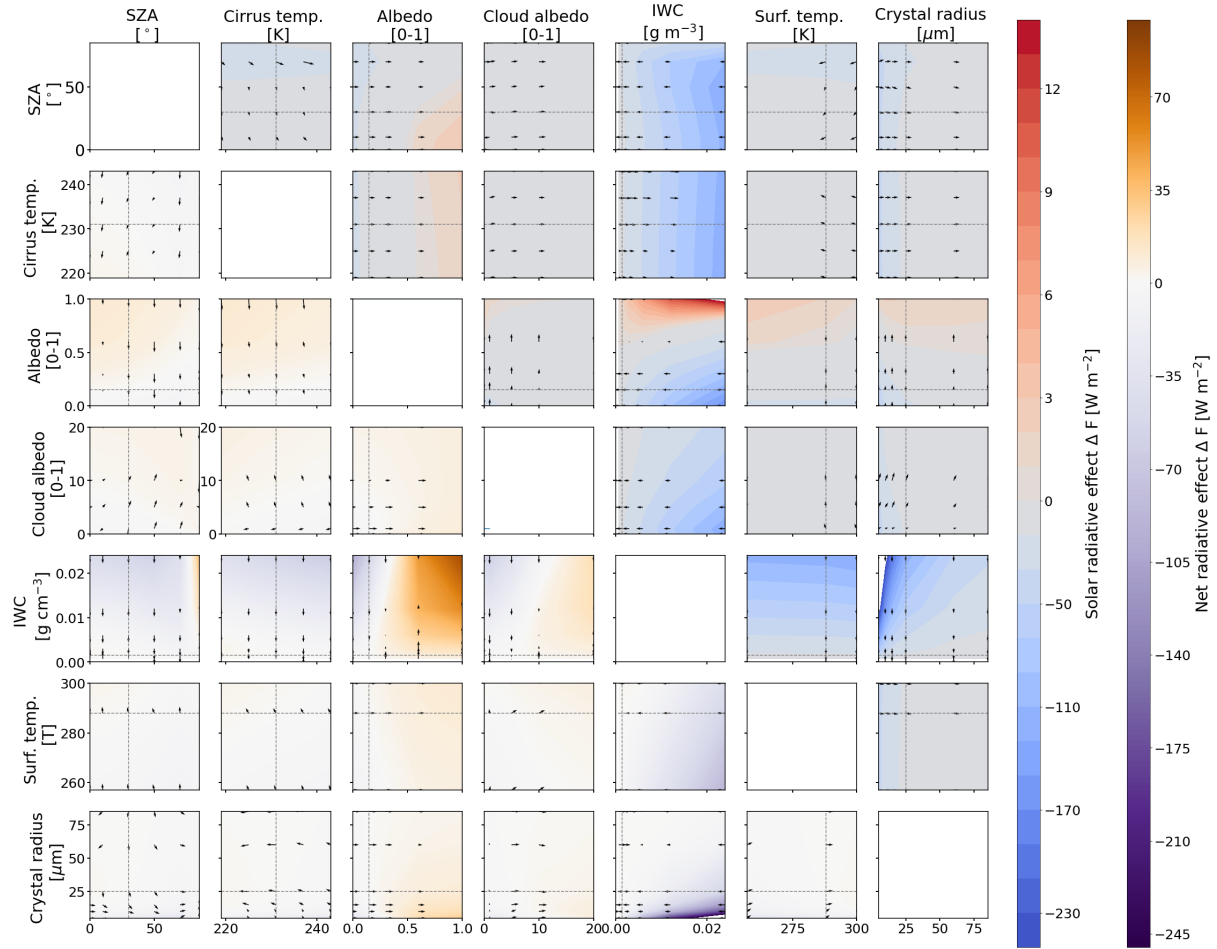
Figure A1. Above diagonal panels: Plot of median solar ΔF_{sol} projected in two-dimensional parameter space. Blue colors indicate negative ΔF_{sol} (cooling), while red colors indicate positive ΔF_{sol} (warming). Below diagonal panels: Same as above diagonal but for median net ΔF_{net}. Purple shades indicate negative ΔF_{net} (cooling), while orange shades indicate positive ΔF_{net} (warming). All ΔF are given in $\mathrm{W\,m^{-2}}$. The black arrows point to the direction of the steepest slope.

depends on the units of the parameters. Therefore, the arrows are normalized and can only be interpreted for their direction and not for their length.

Appendix B: Atmospheric profiles of temperature and relative humidity

The radiative transfer simulations within the present study use the atmospheric profiles from Anderson et al. (1986) that are provided in the libRadtran package. To cover a wide range of temperature conditions, three atmospheric profiles were selected, which represent subarctic, mid-latitude, and tropical conditions given by the `afglsw`, `afglus`, and `afglt` profiles,
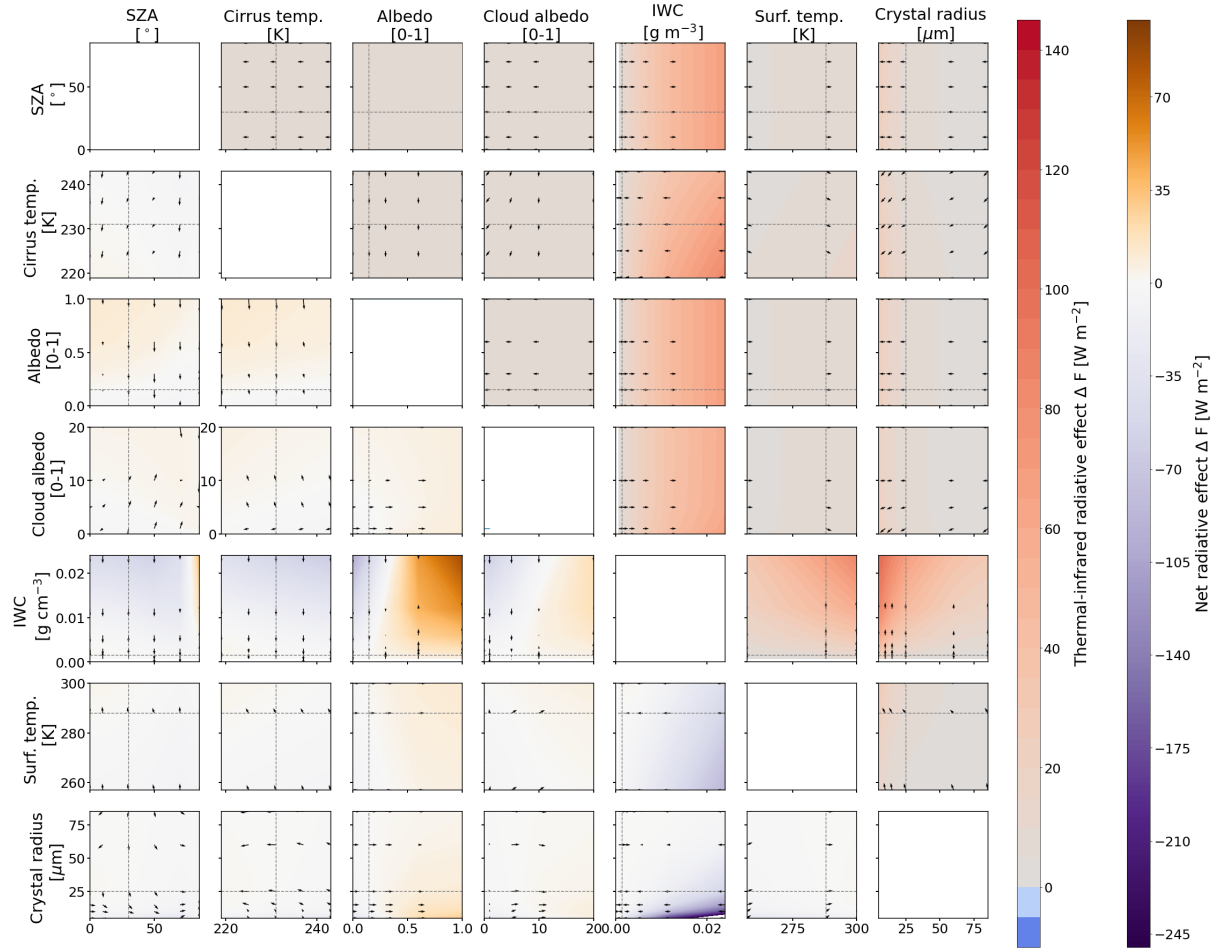
Figure A2. Same as Fig. A1 but above diagonal panels present median ΔF_{tir}. All ΔF are given in $\mathrm{W\,m^{-2}}$.

respectively. The vertical temperature profiles range from 0 to 120 km and are visualized in Fig. B1a. Figure B1b presents a close-up and Fig. B1c shows the relative humidity profile for 0 to 20 km. The position of the low-level liquid water cloud between 1000 and 1500 m is indicated by the gray shaded area. The positions of the ice cloud altitude are indicated by the colored dots.

780 According to Anderson et al. (1986) the presented profiles are subject to variations between 10 % and 30 %. Therefore, we multiplied the original profiles profiles by factors of 0.8 and 1.2 to: i) partly account for this variation and ii) to estimate the influence of variations in RH on the simulated solar, TIR, and net RE. The modified profiles with $\pm 20\,\%$ are indicated by pale colors in Fig B1c.
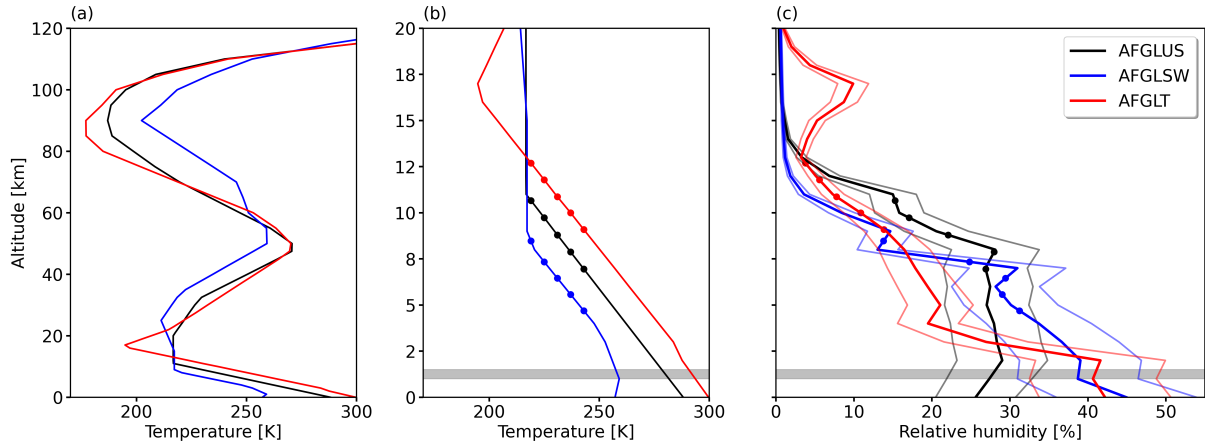
Figure B1. Profiles of temperature (a,b) and relative humidity (c) used for the radiative transfer simulations. The subarctic (`afglsw`), mid-latitude (`afglus`), and tropical (`afglt`) profiles are given in blue, black, and red, respectively. The modified profiles with $\pm 20\%$ are indicated by pale colors. The positions of the simulated ice water cloud are indicated by the colored dots for each profile. The position of the low-level liquid water cloud is indicated by the gray shaded area.

Appendix C: Simulation time and accuracy

The radiative transfer solver DISORT (Stamnes et al., 1988; Buras et al., 2011) allows to select $2N$-number of streams to be used in the radiative transfer simulations. Higher number of streams increases the accuracy of the simulations but also the computational time. To obtain sufficient accuracy while keeping the computational time reasonable, the optimal trade-off was estimated by progressively increasing the number of streams from 4 to 48. The simulation with 48 streams is regarded here as the reference with the highest accuracy and computational time.

The number of streams and the timing of the RT simulations are estimated on the basis of a specific parameter combination, representing a complex cloud scene that is characterized by cloud–cloud–surface-interactions. The simulations are run for a solar zenith angle $\theta = 70°$, a cirrus temperature $T_{\mathrm{cld,ice}}$ of 233 K, a surface albedo $\alpha_{\mathrm{srf}} = 1$, an ice water content IWC = 0.0024 g m^{-3}, a surface temperature $T_{\mathrm{srf}} = 288$ K, an ice crystal effective radius $r_{\mathrm{eff}} = 5\,\mu$m, and an additionally underlying liquid water cloud (cloud optical thickness τ_{liq} = 10).

The computational time that is required for the simulations depends on the available hardware. Therefore, we provide the fraction of the computational time required for n streams to a simulation with 48 streams. The accuracy is given as the relative difference between the cloud RE for a given number of streams with respect to the reference simulation.

Figure C1 shows that the relative difference in the RE decreases with increasing number of streams (higher accuracy). A significant gain in accuracy is achieved by switching from 4 to 10 streams. For simulations with 12 to 16 streams the relative difference remains constant at around 0.1 %. Further increasing to 24 streams provides only a slight gain in accuracy, whereas computational time increases disproportionaly. Therefore, the optimal trade-off between accuracy and computational time is obtained with 16 streams, which is the configuration used in this study.
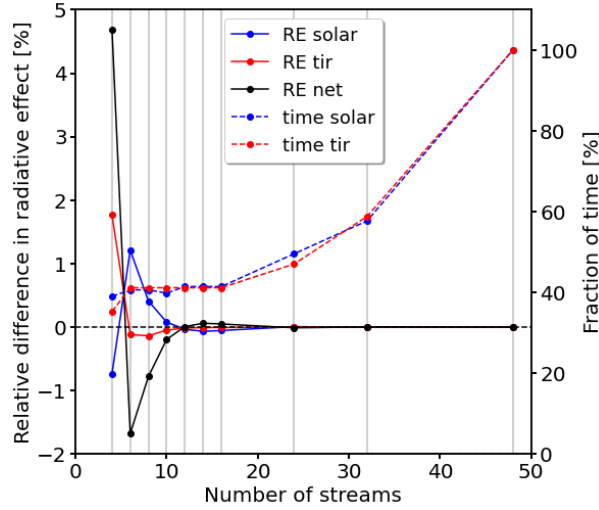
Figure C1. Relative deviation (in %) of solar (solid blue), TIR (solid red), and net (solid black) cloud radiative effect from the reference simulation calculated with 48 streams. The computational time is given as a fraction of the computational time needed for the solar (dashed blue) or TIR (dashed red) simulations using the maximum number of 48 streams.

Appendix D: Single-scattering phase function $\mathcal{P}$

805 The shape-effect is primarily caused by differences in the extinction of radiation and the asymmetry parameter. The asymmetry parameter is a measure of the asymmetry of the phase function $\mathcal{P}$ between forward and backward scattering (Macke et al., 1998; Fu, 2007). $\mathcal{P}$ provides the angular distribution of the scattered direction in relation to the incident light. As an example, Fig. D1a–d shows $\mathcal{P}$ at 550 nm wavelength for columns; plates; droxtals; and Yang's '8–column_aggregates', which are ice crystals consisting of 8 merged columns. The phase functions are extracted from the post-processed libRadtran data set that is

810 based on the ice optics computations from Yang et al. (2013).

All ice crystal shapes are characterized by a dominating peak in the forward direction, which drops by a factor of 10^4 sr^{-1}, when the scattering angle Θ increases from $0°$ to $10°$. For $10° < \Theta < 160°$, $\mathcal{P}$ varies between 10^{-1} sr^{-1} and 10^1 sr^{-1}. Towards $\Theta > 160°$ the phase function increases, showing enhanced backward scattering except for the complex shaped crystals (Fig. D1d). Further characteristics of $\mathcal{P}$ are local maxima at $22°$ scattering angles and cause halo phenomena. Additionally,

815 non-spherical crystals (Fig. D1a,b,d) have enhanced sideward scattering compared to ice crystals with a roughly spherical shape, like droxtals (Fig. D1c) or water droplets. Another characteristic is the shift in the $\mathcal{P}$ from variations in the crystal radius r_{eff}, which is most prominent for plates and lowest for columns.

Author contributions. **KW** designed the model setup, conducted the experiments and the data analysis, and prepared the manuscript. **NB** and **OB** contributed equally to the analysis and the preparation of the manuscript.
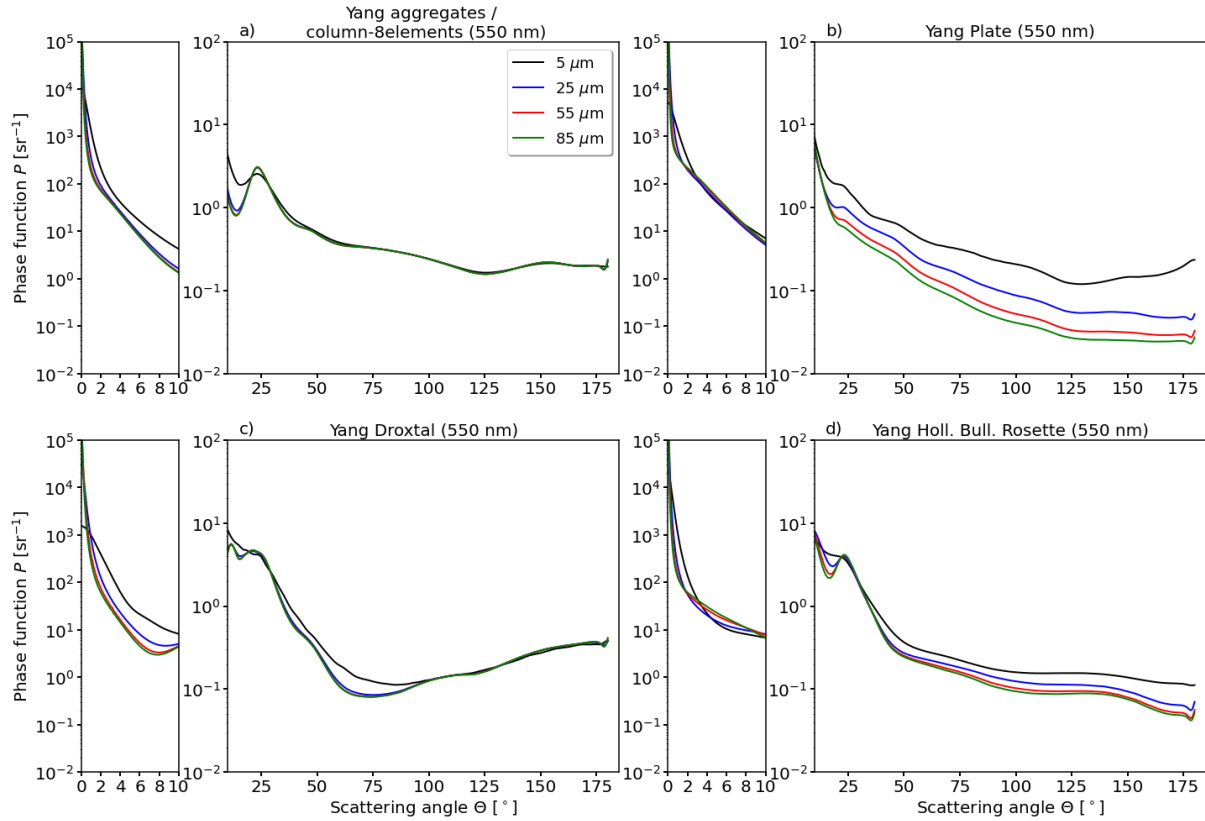
Figure D1. Phase function of four different ice crystal shapes with moderate surface roughness and four particle size distributions at 550 nm wavelength. Please note the two different y-scales to account for the different magnitudes in the forward scattering peak. Plotted $\mathcal{P}$ are post-processed phase functions from Emde et al. (2016) that are based on Yang et al. (2013). The phase functions from Emde et al. (2016) assume a crystal size distribution that follows a gamma function.

820   *Competing interests.*   The authors declare no competing interest.

Acknowledgements.   The authors acknowledge support from the Direction Générale de l'Aviation Civile through the Convention N°2021-39 relative to "Aviation & Climate". We further would like to thank David L. Mitchell, Andreas Macke, and one anonymous reviewer for their insightful comments during the review that improved and strengthened the manuscript, and Matthias Tesche for serving as editor.

References

825   Anderson, G. P., Clough, S. A., Kneizys, F. X., Chetwynd, J. H., and Shettle, E. P.: AFGL atmospheric constituent profiles, Environ. Res. Pap, 954, 1–46, 1986.

Baldridge, A. M., Hook, S. J., Grove, C. I., and Rivera, G.: The ASTER spectral library version 2.0, Remote Sens. Environ., 113, 711–715, https://doi.org/10.1016/j.rse.2008.11.007, 2009.

Bauer, P., Thorpe, A., and Brunet, G.: The quiet revolution of numerical weather prediction., Nature, 525, 47–55, https://doi.org/10.1038/nature14956, 2015.

830

Baum, B. A., Heymsfield, A. J., Yang, P., and Bedka, S. T.: Bulk scattering properties for the remote sensing of ice clouds. Part I: microphysical data and models, J. Appl. Meteorol., 44, 1885–1895, https://doi.org/10.1175/JAM2308.1, 2005a.

Baum, B. A., Yang, P., Heymsfield, A. J., Platnick, S., King, M. D., Hu, Y.-X., and Bedka, S. T.: Bulk scattering properties for the remote sensing of ice clouds. Part II: narrowband models, J. Appl. Meteorol., 44, 1896–1911, https://doi.org/10.1175/JAM2309.1, 2005b.

835   Baum, B. A., Yang, P., Nasiri, S., Heidinger, A. K., Heymsfield, A., and Li, J.: Bulk scattering properties for the remote sensing of ice clouds. Part III: high-resolution spectral models from 100 to 3250 cm-1, J. Appl. Meteorol., 46, 423–434, https://doi.org/10.1175/JAM2473.1, 2007.

Bi, L., Yang, P., Liu, C., Yi, B., Baum, B. A., van Diedenhoven, B., and Iwabuchi, H.: Assessment of the accuracy of the conventional ray-tracing technique: Implications in remote sensing and radiative transfer involving ice clouds, J. Quant. Spectrosc. Radiat. Transfer,

840   146, 158–174, https://doi.org/10.1016/j.jqsrt.2014.03.017, 2014.

Bickel, M., Ponater, M., Bock, L., Burkhardt, U., and Reineke, S.: Estimating the effective radiative forcing of contrail cirrus, J. Climate, 33, 1991–2005, https://doi.org/10.1175/JCLI-D-19-0467.1, 2020.

Bräuer, T., Voigt, C., Sauer, D., Kaufmann, S., Hahn, V., Scheibe, M., Schlager, H., Diskin, G. S., Nowak, J. B., DiGangi, J. P., Huber, F., Moore, R. H., and Anderson, B. E.: Airborne measurements of contrail ice properties–dependence on temperature and humidity, Geophys.

845   Res. Lett., 48, e2020GL092 166, https://doi.org/10.1029/2020GL092166, 2021.

Buras, R., Dowling, T., and Emde, C.: New secondary-scattering correction in DISORT with increased efficiency for forward scattering, J. Quant. Spectrosc. Radiat. Transfer, 112, 2028–2034, https://doi.org/10.1016/j.jqsrt.2011.03.019, 2011.

Burkhardt, U. and Kärcher, B.: Global radiative forcing from contrail cirrus, Nat. Clim. Change, 1, 54–58, https://doi.org/10.1038/nclimate1068, 2011.

850   Cahalan, R. F., Ridgway, W., Wiscombe, W. J., Bell, T. L., and Snider, J. B.: The albedo of fractal stratocumulus clouds, J. Atmos. Sci., 51, 2434–2455, https://doi.org/10.1175/1520-0469(1994)051<2434:TAOFSC>2.0.CO;2, 1994.

Campbell, J. R., Lolli, S., Lewis, J. R., Gu, Y., and Welton, E. J.: Daytime cirrus cloud top-of-the-atmosphere radiative forcing properties at a midlatitude site and their global consequences, J. Appl. Meteorology and Climatology, 55, 1667–1679, https://doi.org/10.1175/JAMC-D-15-0217.1, 2016.

855   Chen, T., Rossow, W. B., and Zhang, Y.: Radiative effects of cloud-type variations, J. Climate, 13, 264–286, https://doi.org/10.1175/1520-0442(2000)013<0264:REOCTV>2.0.CO;2, 2000.

Coakley, J. A. and Chylek, P.: The two-stream approximation in radiative rransfer: including the angle of the incident radiation, J. Atmos. Sci., 32, 409–418, https://doi.org/10.1175/1520-0469(1975)032<0409:TTSAIR>2.0.CO;2, 1975.

Corti, T. and Peter, T.: A simple model for cloud radiative forcing, Atmos. Chem. Phys., 9, 5751–5758, https://doi.org/10.5194/acp-9-5751-

860   2009, 2009.

Deirmendjian, D.: Scattering and polarization properties of polydispersed suspensions with partial absorption, Tech. rep., RAND CORP SANTA MONICA CA, 1962.

Emde, C., Buras-Schnell, R., Kylling, A., Mayer, B., Gasteiger, J., Hamann, U., Kylling, J., Richter, B., Pause, C., Dowling, T., and Bugliaro, L.: The libRadtran software package for radiative transfer calculations (version 2.0.1), Geosci. Model Dev., 9, 1647–1672, https://doi.org/10.5194/gmd-9-1647-2016, 2016.

Evans, K. F.: The spherical harmonics discrete ordinate method for three-dimensional atmospheric radiative transfer, J. Atmos. Sci., 55, 429–446, https://doi.org/10.1175/1520-0469(1998)055<0429:TSHDOM>2.0.CO;2, 1998.

Fahey, D. W., Schumann, U., Ackerman, S., Artaxo, P., Boucher, O., Danilin, M. Y., Kärcher, B., Minnis, P., Nakajima, T., and Toon, O. B.: Aviation-produced aerosols and cloudiness. IPCC special report., pp. 65–120, 1999.

Fauchez, T., Platnick, S., Meyer, K., Cornet, C., Szczap, F., and Várnai, T.: Scale dependence of cirrus horizontal heterogeneity effects on TOA measurements – Part I: MODIS brightness temperatures in the thermal infrared, Atmos. Chem. Phys., 17, 8489–8508, https://doi.org/10.5194/acp-17-8489-2017, 2017.

Fauchez, T., Platnick, S., Várnai, T., Meyer, K., Cornet, C., and Szczap, F.: Scale dependence of cirrus heterogeneity effects. Part II: MODIS NIR and SWIR channels, Atmos. Chem. Phys., 18, 12 105–12 121, https://doi.org/10.5194/acp-18-12105-2018, 2018.

Forster, L. and Mayer, B.: Ice crystal characterization in cirrus clouds III: retrieval of ice crystal shape and roughness from observations of halo displays, Atmos. Chem. Phys., 22, 15 179–15 205, https://doi.org/10.5194/acp-22-15179-2022, 2022.

Forster, L., Emde, C., Mayer, B., and Unterstrasser, S.: Effects of three-dimensional photon transport on the radiative forcing of realistic contrails, J. Atmos. Sci., 69, 2243–2255, https://doi.org/10.1175/JAS-D-11-0206.1, 2012.

Forster, L., Seefeldner, M., Wiegner, M., and Mayer, B.: Ice crystal characterization in cirrus clouds: a sun-tracking camera system and automated detection algorithm for halo displays, Atmos. Meas. Tech., 10, 2499–2516, https://doi.org/10.5194/amt-10-2499-2017, 2017.

Freudenthaler, V., Homburg, F., and Jäger, H.: Contrail observations by ground-based scanning lidar: Cross-sectional growth, Geophys. Res. Lett., 22, 3501–3504, https://doi.org/10.1029/95GL03549, 1995.

Freudenthaler, V., Homburg, F., and Jäger, H.: Optical parameters of contrails from lidar measurements: Linear depolarization, Geophys. Res. Lett., 23, 3715–3718, https://doi.org/10.1029/96GL03646, 1996.

Fu, Q.: An accurate parameterization of the solar radiative properties of cirrus clouds for climate models, J. Climate, 9, 2058–2082, https://doi.org/10.1175/1520-0442(1998)011<2223:AAPOTI>2.0.CO;2, 1996.

Fu, Q.: A new parameterization of an asymmetry factor of cirrus clouds for climate models, J. Atmos. Sci., 64, 4140–4150, https://doi.org/10.1175/2007JAS2289.1, 2007.

Fu, Q. and Liou, K. N.: Parameterization of the radiative properties of cirrus clouds, J. Atmos. Sci., 50, 2008–2025, https://doi.org/10.1175/1520-0469(1993)050<2008:POTRPO>2.0.CO;2, 1993.

Gardner, A. S. and Sharp, M. J.: A review of snow and ice albedo and the development of a new physically based broadband albedo parameterization, J. Geophys. Res. Earth Surf., 115, F01 009, https://doi.org/10.1029/2009JF001444, 2010.

Gasteiger, J., Emde, C., Mayer, B., Buras, R., Buehler, S., and Lemke, O.: Representative wavelengths absorption parameterization applied to satellite channels and spectral bands, J. Quant. Spectrosc. Radiat. Transfer, 148, 99–115, https://doi.org/10.1016/j.jqsrt.2014.06.024, 2014.

Gayet, J.-F., Shcherbakov, V., Voigt, C., Schumann, U., Schäuble, D., Jessberger, P., Petzold, A., Minikin, A., Schlager, H., Dubovik, O., and Lapyonok, T.: The evolution of microphysical and optical properties of an A380 contrail in the vortex phase, Atmos. Chem. Phys., 12, 6629–6643, https://doi.org/10.5194/acp-12-6629-2012, 2012.

Glickman, T. S.: Glossary of Meteorology, American Meteorological Society, 2nd edn., 2000.

900 Goodman, J., Pueschel, R. F., Jensen, E. J., Verma, S., Ferry, G. V., Howard, S. D., Kinne, S. A., and Baumgardner, D.: Shape and size of contrails ice particles, Geophys. Res. Lett., 25, 1327–1330, https://doi.org/10.1029/97GL03091, 1998.

Gounou, A. and Hogan, R. J.: A sensitivity study of the effect of horizontal photon transport on the radiative forcing of contrails, J. Atmos. Sci., 64, 1706–1716, https://doi.org/10.1175/JAS3915.1, 2007.

Gueymard, C. A., Lara-Fanego, V., Sengupta, M., and Xie, Y.: Surface albedo and reflectance: Review of definitions, angular and spectral

905 effects, and intercomparison of major data sources in support of advanced solar irradiance modeling over the Americas, Sol. Energy, 182, 194–212, https://doi.org/10.1016/j.solener.2019.02.040, 2019.

Hansen, J. E. and Travis, L. D.: Light scattering in planetary atmospheres, Space Sci. Rev., 16, 527—-610, https://doi.org/10.1007/BF00168069, 1974.

Haywood, J. M. and Shine, K. P.: Multi-spectral calculations of the direct radiative forcing of tropospheric sulphate and soot aerosols using

910 a column model, Q. J. Royal Meteorol. Soc., 123, 1907–1930, https://doi.org/10.1002/qj.49712354307, 1997.

Haywood, J. M., Allan, R. P., Bornemann, J., Forster, P. M., Francis, P. N., Milton, S., Rädel, G., Rap, A., Shine, K. P., and Thorpe, R.: A case study of the radiative forcing of persistent contrails evolving into contrail-induced cirrus, J. Geophys. Res. Atmos., 114, D24 201, https://doi.org/10.1029/2009JD012650, 2009.

Heymsfield, A. J., Bansemer, A., Field, P. R., Durden, S. L., Stith, J. L., Dye, J. E., Hall, W., and Grainger, C. A.: Observations and

915 parameterizations of particle size distributions in deep tropical cirrus and stratiform precipitating clouds: results from in situ observations in TRMM field campaigns, J. Atmos. Sci., 59, 3457–3491, https://doi.org/10.1175/1520-0469(2002)059<3457:OAPOPS>2.0.CO;2, 2002.

Hogan, R. J., Behera, M. D., O'Connor, E. J., and Illingworth, A. J.: Estimate of the global distribution of stratiform supercooled liquid water clouds using the LITE lidar, Geophys. Res. Lett., 31, https://doi.org/10.1029/2003GL018977, 2004.

Holz, R. E., Platnick, S., Meyer, K., Vaughan, M., Heidinger, A., Yang, P., Wind, G., Dutcher, S., Ackerman, S., Amarasinghe, N., Nagle, F.,

920 and Wang, C.: Resolving ice cloud optical thickness biases between CALIOP and MODIS using infrared retrievals, Atmos. Chem. Phys., 16, 5075–5090, https://doi.org/10.5194/acp-16-5075-2016, 2016.

Horváth, A. and Davies, R.: Comparison of microwave and optical cloud water path estimates from TMI, MODIS, and MISR, J. Geophys. Res. Atmos., 112, D01 202, https://doi.org/10.1029/2006JD007101, 2007.

Hu, Y., Rodier, S., Xu, K., Sun, W., Huang, J., Lin, B., Zhai, P., and Josset, D.: Occurrence, liquid water content, and fraction of supercooled

925 water clouds from combined CALIOP/IIR/MODIS measurements, J. Geophys. Res. Atmos., 115, https://doi.org/10.1029/2009JD012384, 2010.

Iwabuchi, H., Yang, P., Liou, K. N., and Minnis, P.: Physical and optical properties of persistent contrails: Climatology and interpretation, J. Geophys. Res. Atmos., 117, D06 215, https://doi.org/10.1029/2011JD017020, 2012.

Järvinen, E., Jourdan, O., Neubauer, D., Yao, B., Liu, C., Andreae, M. O., Lohmann, U., Wendisch, M., McFarquhar, G. M., Leisner, T.,

930 and Schnaiter, M.: Additional global climate cooling by clouds due to ice crystal complexity, Atmos. Chem. Phys., 18, 15 767–15 781, https://doi.org/10.5194/acp-18-15767-2018, 2018.

Jeßberger, P., Voigt, C., Schumann, U., Sölch, I., Schlager, H., Kaufmann, S., Petzold, A., Schäuble, D., and Gayet, J.-F.: Aircraft type influence on contrail properties, Atmos. Chem. Phys., 13, 11 965–11 984, https://doi.org/10.5194/acp-13-11965-2013, 2013.

Kahnert, M., Sandvik, A. D., Biryulina, M., Stamnes, J. J., and Stamnes, K.: Impact of ice particle shape on short-wave radiative forcing:

935 A case study for an arctic ice cloud, J. Quant. Spectrosc. Radiat. Transfer, 109, 1196–1218, https://doi.org/10.1016/j.jqsrt.2007.10.016, 2008.

Kärcher, B.: Formation and radiative forcing of contrail cirrus, Nat. Commun., 7, https://doi.org/10.1038/s41467-018-04068-0, 2018.

Key, J. R., Yang, P., Baum, B. A., and Nasiri, S. L.: Parameterization of shortwave ice cloud optical properties for various particle habits, J. Geophys. Res. Atmos., 107, AAC 7–1–AAC 7–10, https://doi.org/https://doi.org/10.1029/2001JD000742, 2002.

940 Krämer, M., Rolf, C., Luebke, A., Afchine, A., Spelten, N., Costa, A., Meyer, J., Zöger, M., Smith, J., Herman, R. L., Buchholz, B., Ebert, V., Baumgardner, D., Borrmann, S., Klingebiel, M., and Avallone, L.: A microphysics guide to cirrus clouds – Part 1: Cirrus types, Atmos. Chem. Phys., 16, 3463–3483, https://doi.org/10.5194/acp-16-3463-2016, 2016.

Krämer, M., Rolf, C., Spelten, N., Afchine, A., Fahey, D., Jensen, E., Khaykin, S., Kuhn, T., Lawson, P., Lykov, A., Pan, L. L., Riese, M., Rollins, A., Stroh, F., Thornberry, T., Wolf, V., 945 Woods, S., Spichtinger, P., Quaas, J., and Sourdeval, O.: A microphysics guide to cirrus – Part 2: Climatologies of clouds and humidity from observations, Atmos. Chem. Phys., 20, 12 569–12 608, https://doi.org/10.5194/acp-20-12569-2020, 2020.

Kurucz, R. L.: Synthetic infrared spectra, Infrared solar physics: proceedings of the 154th Symposium of the International Astronomical Union, 1992.

950 Lawson, R. P., Heymsfield, A. J., Aulenbach, S. M., and Jensen, T. L.: Shapes, sizes and light scattering properties of ice crystals in cirrus and a persistent contrail during SUCCESS, Geophys. Res. Lett., 25, 1331–1334, https://doi.org/10.1029/98GL00241, 1998.

Lee, D. S., Fahey, D. W., Skowron, A., Allen, M. R., Burkhardt, U., Chen, Q., Doherty, S. J., Freeman, S., Forster, P. M., Fuglestvedt, J., Gettelman, A., De León, R. R., Lim, L. L., Lund, M. T., Millar, R. J., Owen, B., Penner, J. E., Pitari, G., Prather, M. J., Sausen, R., and Wilcox, L. J.: The contribution of global aviation to anthropogenic climate forcing for 2000 to 2018, Atmos. Environ., 244, 117 834, 955 https://doi.org/10.1016/j.atmosenv.2020.117834, 2021.

Liou, K.-N.: Influence of cirrus clouds on weather and climate processes: A global perspective, Mon. Weather Rev., 114, 1167–1199, https://doi.org/10.1175/1520-0493(1986)114<1167:IOCCOW>2.0.CO;2, 1986.

Liou, K. N.: Radiation and cloud processes in the atmosphere. Theory, observation, and modeling, Oxford University Press, 1992.

Liu, C., Yang, P., Minnis, P., Loeb, N., Kato, S., Heymsfield, A., and Schmitt, C.: A two-habit model for the microphysical and optical 960 properties of ice clouds, Atmos. Chem. Phys., 14, 13 719–13 737, https://doi.org/10.5194/acp-14-13719-2014, 2014.

Luebke, A. E., Afchine, A., Costa, A., Grooß, J.-U., Meyer, J., Rolf, C., Spelten, N., Avallone, L. M., Baumgardner, D., and Krämer, M.: The origin of midlatitude ice clouds and the resulting influence on their microphysical properties, Atmos. Chem. Phys., 16, 5793–5809, https://doi.org/10.5194/acp-16-5793-2016, 2016.

Luebke, A. E., Ehrlich, A., Schäfer, M., Wolf, K., and Wendisch, M.: An assessment of macrophysical and microphysical cloud properties 965 driving radiative forcing of shallow trade-wind clouds, Atmos. Chem. Phys., 22, 2727–2744, https://doi.org/10.5194/acp-22-2727-2022, 2022.

Lynch, D. K., Sassen, K., Starr, D. O., and Stephens, G.: Cirrus, chap. 2, Oxford University Press, 1 edn., 2002.

Macke, A., Mishchenko, M. I., and Cairns, B.: The influence of inclusions on light scattering by large ice particles, J. Geophys. Res. Atmos., 101, 23 311–23 316, https://doi.org/10.1029/96JD02364, 1996a.

970 Macke, A., Mueller, J., and Raschke, E.: Single scattering properties of atmospheric ice crystals, J. Atmos. Sci., 53, 2813–2825, https://doi.org/10.1175/1520-0469(1996)053<2813:SSPOAI>2.0.CO;2, 1996b.

Macke, A., Francis, P. N., McFarquhar, G. M., and Kinne, S.: The role of ice particle shapes and size distributions in the single scattering properties of cirrus clouds, J. Atmos. Sci., 55, 2874–2883, https://doi.org/10.1175/1520-0469(1998)055<2874:TROIPS>2.0.CO;2, 1998.

Markowicz, K. M. and Witek, M. L.: Simulations of contrail optical properties and radiative forcing for various cystal shapes, J. Appl. Meteor. Climatol., 50, 1740–1755, https://doi.org/10.1175/2011JAMC2618.1, 2011.

McFarquhar, G. M., Zhang, G., Poellot, M. R., Kok, G. L., McCoy, R., Tooman, T., Fridlind, A., and Heymsfield, A. J.: Ice properties of single-layer stratocumulus during the mixed-phase Arctic cloud experiment: 1. Observations, J. Geophys. Res. Atmos., 112, D24 201, https://doi.org/10.1029/2007JD008633, 2007.

Medeiros, B., Nuijens, L., Antoniazzi, C., and Stevens, B.: Low-latitude boundary layer clouds as seen by CALIPSO, J. Geophys. Res. Atmos., 115, D23 207, https://doi.org/10.1029/2010JD014437, 2010.

Meerdink, S. K., Hook, S. J., Roberts, D. A., and Abbott, E. A.: The ECOSTRESS spectral library version 1.0, Remote Sens. Environ., 230, 111 196, https://doi.org/10.1016/j.rse.2019.05.015, 2019.

Meerkötter, R., Schumann, U., Doelling, D. R., Minnis, P., Nakajima, T., and Tsushima, Y.: Radiative forcing by contrails, Ann. Geophys., 17, 1080–1094, https://doi.org/10.1007/s00585-999-1080-7, 1999.

Mie, G.: Beiträge zur Optik trüber Medien, speziell kolloidaler Metallösungen, Ann. Phys., 330, 377–445, https://doi.org/10.1002/andp.19083300302, 1908.

Minnis, P., Schumann, U., Doelling, D. R., Gierens, K. M., and Fahey, D. W.: Global distribution of contrail radiative forcing, Geophys. Res. Lett., 26, 1853–1856, https://doi.org/10.1029/1999GL900358, 1999.

Mishchenko, M. I.: Comprehensive thematic T-matrix reference database: a 2017–2019 update, J. Quant. Spectrosc. Radiat. Transfer, 242, 106 692, https://doi.org/10.1016/j.jqsrt.2019.106692, 2020.

Mitchell, D., Huggins, A., and Grubisic, V.: A new snow growth model with application to radar precipitation estimates, Atmos. Res., 82, 2–18, https://doi.org/10.1016/j.atmosres.2005.12.004, 14th International Conference on Clouds and Precipitation, 2006.

Mitchell, D. L.: Use of mass- and area-dimensional power laws for determining precipitation particle terminal velocities, J. Atmos. Sci., 53, 1710–1723, https://doi.org/10.1175/1520-0469(1996)053<1710:UOMAAD>2.0.CO;2, 1996.

Mitchell, D. L.: Effective diameter in radiation transfer: general definition, applications, and limitations, J. Atmos. Sci., 59, 2330–2346, https://doi.org/10.1175/1520-0469(2002)059<2330:EDIRTG>2.0.CO;2, 2002.

Mitchell, D. L., Lawson, R. P., and Baker, B.: Understanding effective diameter and its application to terrestrial radiation in ice clouds, Atmos. Chem. Phys., 11, 3417–3429, https://doi.org/10.5194/acp-11-3417-2011, 2011.

Muhlbauer, A., McCoy, I. L., and Wood, R.: Climatology of stratocumulus cloud morphologies: microphysical properties and radiative effects, Atmos. Chem. Phys., 14, 6695–6716, https://doi.org/10.5194/acp-14-6695-2014, 2014.

Myhre, G. and Stordal, F.: On the tradeoff of the solar and thermal infrared radiative impact of contrails, Geophys. Res. Let., 28, 3119–3122, https://doi.org/10.1029/2001GL013193, 2001.

Nazaryan, H., McCormick, M. P., and Menzel, W. P.: Global characterization of cirrus clouds using CALIPSO data, J. Geophys. Res. Atmos., 113, D16 211, https://doi.org/10.1029/2007JD009481, 2008.

Noël, V. and Haeffelin, M.: Midlatitude cirrus clouds and multiple tropopauses from a 2002–2006 climatology over the SIRTA observatory, J. Geophys. Res. Atmos., 112, https://doi.org/10.1029/2006JD007753, 2007.

Petty, G. W. and Huang, W.: The modified gamma size distribution applied to inhomogeneous and nonspherical particles: Key relationships and conversions, J. Atmos. Sci., 68, 1460–1473, https://doi.org/10.1175/2011JAS3645.1, 2011.

Petzold, A., Busen, R., Schröder, F. P., Baumann, R., Kuhn, M., Ström, J., Hagen, D. E., Whitefield, P. D., Baumgardner, D., Arnold, F., Borrmann, S., and Schumann, U.: Near-field measurements on contrail properties from fuels with different sulfur content, J. Geophys. Res. Atmos., 102, 29 867–29 880, https://doi.org/10.1029/97JD02209, 1997.

Platnick, S., Meyer, K. G., King, M. D., Wind, G., Amarasinghe, N., Marchant, B., Arnold, G. T., Zhang, Z., Hubanks, P. A., Holz, R. E., Yang, P., Ridgway, W. L., and Riedi, J.: The MODIS cloud optical and microphysical products: Collection 6 updates and examples from Terra and Aqua, IEEE Trans. Geosci. Remote. Sens., 55, 502–525, https://doi.org/10.1109/TGRS.2016.2610522, 2017.

Quaas, J., Gryspeerdt, E., Vautard, R., and Boucher, O.: Climate impact of aircraft-induced cirrus assessed from satellite observations before and during COVID-19, Environ. Res. Let., 16, 064 051, https://doi.org/10.1088/1748-9326/abf686, 2021.

Ramanathan, V., Cess, R. D., Harrison, E. F., Minnis, P., Barkstrom, B. R., Ahmad, E., and Hartmann, D.: Cloud-radiative forcing and climate: Results from the Earth radiation budget experiment, Science, 243, 57–63, http://www.jstor.org/stable/1703174, 1989.

Rémillard, J., Kollias, P., Luke, E., and Wood, R.: Marine boundary layer cloud observations in the Azores, J. Clim., 25, 7381–7398, https://doi.org/10.1175/JCLI-D-11-00610.1, 2012.

Sanz-Morère, I., Eastham, S. D., Allroggen, F., Speth, R. L., and Barrett, S. R. H.: Impacts of multi-layer overlap on contrail radiative forcing, Atmos. Chem. Phys., 21, 1649–1681, https://doi.org/10.5194/acp-21-1649-2021, 2021.

Sassen, K.: Contrail-cirrus and their potential for regional climate change, Bull. Am. Meteorol. Soc., 78, 1885–1904, https://doi.org/10.1175/1520-0477(1997)078<1885:CCATPF>2.0.CO;2, 1997.

Sassen, K. and Campbell, J. R.: A midlatitude cirrus cloud climatology from the facility for atmospheric remote sensing. Part I: macrophysical and synoptic properties, J. Atmos. Sci., 58, 481–496, https://doi.org/10.1175/1520-0469(2001)058<0481:AMCCCF>2.0.CO;2, 2001.

Sassen, K., Wang, Z., and Liu, D.: Global distribution of cirrus clouds from CloudSat/Cloud-Aerosol Lidar and Infrared Pathfinder Satellite Observations (CALIPSO) measurements, J. Geophys. Res. Atmos., 113, D00A12, https://doi.org/10.1029/2008JD009972, 2008.

Schröder, F., Kärcher, B., Duroure, C., Ström, J., Petzold, A., Gayet, J.-F., Strauss, B., Wendling, P., and Borrmann, S.: On the transition of contrails into cirrus clouds, J. Atmos. Sci., 57, 464–480, https://doi.org/10.1175/1520-0469(2000)057<0464:OTTOCI>2.0.CO;2, 2000.

Schulz, J.: On the effect of cloud inhomogeneity an area averaged radiative properties of contrails, Geophys. Res. Lett., 25, 1427–1430, https://doi.org/10.1029/98GL51098, 1998.

Schumann, U.: On conditions for contrail formation from aircraft exhausts, Meteorologische Zeitschrift, 5, 1996.

Schumann, U.: A contrail cirrus prediction model, Geosci. Model Dev., 5, 543–580, https://doi.org/10.5194/gmd-5-543-2012, 2012.

Schumann, U. and Heymsfield, A. J.: On the life cycle of individual contrails and contrail cirrus, Meteorol. Monogr., 58, 3.1–3.24, https://doi.org/10.1175/AMSMONOGRAPHS-D-16-0005.1, 2017.

Schumann, U., Mayer, B., Gierens, K., Unterstrasser, S., Jessberger, P., Petzold, A., Voigt, C., and Gayet, J.-F.: Effective radius of ice particles in cirrus and contrails, J. Atmos. Sci., 68, 300–321, https://doi.org/10.1175/2010JAS3562.1, 2011.

Schumann, U., Penner, J. E., Chen, Y., Zhou, C., and Graf, K.: Dehydration effects from contrails in a coupled contrail–climate model, Atmos. Chem. Phys., 15, 11 179–11 199, https://doi.org/10.5194/acp-15-11179-2015, 2015.

Schumann, U., Bugliaro, L., Dörnbrack, A., Baumann, R., and Voigt, C.: Aviation contrail cirrus and radiative forcing over europe during 6 months of COVID-19, Geophys. Res. Lett., 48, https://doi.org/https://doi.org/10.1029/2021GL092771, e2021GL092771 2021GL092771, 2021.

Stamnes, K., Tsay, S.-C., Wiscombe, W., and Jayaweera, K.: Numerically stable algorithm for discrete-ordinate-method radiative transfer in multiple scattering and emitting layered media, Appl. Opt., 27, 2502–2509, https://doi.org/10.1364/AO.27.002502, 1988.

Stapf, J., Ehrlich, A., and Wendisch, M.: Influence of thermodynamic state changes on surface cloud radiative forcing in the Arctic: A comparison of two approaches using data from AFLUX and SHEBA, J. Geophys. Res. Atmos., 126, e2020JD033 589, https://doi.org/10.1029/2020JD033589, 2021.

Stephens, G. L., Tsay, S.-C., Stackhouse, P. W., and Flatau, P. J.: The relevance of the microphysical and radiative properties of cirrus clouds to climate and climatic feedback, J. Atmos. Sci., 47, 1742–1754, https://doi.org/10.1175/1520-0469(1990)047<1742:TROTMA>2.0.CO;2, 1990.

Stephens, G. L., Gabriel, P. M., and Tsay, S.-C.: Statistical radiative transport in one-dimensional media and its application to the terrestrial atmosphere, Transp. Theory Stat. Phys., 20, 139–175, https://doi.org/10.1080/00411459108203900, 1991.

Stephens, G. L., Wood, N. B., and Gabriel, P. M.: An assessment of the parameterization of subgrid-scale cloud effects on radiative transfer. Part I: Vertical overlap, J. Atmos. Sci., 61, 715–732, https://doi.org/10.1175/1520-0469(2004)061<0715:AAOTPO>2.0.CO;2, 2004.

Stevens, B. and Bony, S.: What are climate models missing?, Science, 340, 1053–1054, https://doi.org/10.1126/science.1237554, 2013.

Stevens, B., Farrell, D., Hirsch, L., Jansen, F., Nuijens, L., Serikov, I., Brügmann, B., Forde, M., Linne, H., Lonitz, K., and Prospero, J. M.: The Barbados Cloud Observatory: Anchoring investigations of clouds and circulation on the edge of the ITCZ, Bull. Am. Meteorol. Soc., 97, 787–801, https://doi.org/10.1175/BAMS-D-14-00247.1, 2016.

Strauss, B., Meerkötter, R., Wissinger, B., Wendling, P., and Hess, M.: On the regional climatic impact of contrails: microphysical and radiative properties of contrails and natural cirrus clouds, Ann. Geophys., 15, 1457–1467, https://doi.org/10.1007/s00585-997-1457-4, 1997.

Stuber, N., Forster, P., Rädel, G., and Shine, K.: The importance of the diurnal and annual cycle of air traffic for contrail radiative forcing, Nature, 441, 864—867, https://doi.org/10.1038/nature04877, 2006.

Takano, Y. and Liou, K.-N.: Solar radiative transfer in cirrus clouds. Part I: Single-scattering and optical properties of hexagonal ice crystals, J. Atmos. Sci., 46, 3–19, https://doi.org/10.1175/1520-0469(1989)046<0003:SRTICC>2.0.CO;2, 1989.

Unterstrasser, S. and Stephan, A.: Far field wake vortex evolution of two aircraft formation flight and implications on young contrails, The Aeronaut. J., 124, 667—702, https://doi.org/10.1017/aer.2020.3, 2020.

van de Hulst, H. C.: Light scattering by small particles, Courier Corporation, first edn., 1981.

van Diedenhoven, B., Fridlind, A. M., Ackerman, A. S., Eloranta, E. W., and McFarquhar, G. M.: An evaluation of ice formation in large-eddy simulations of supercooled Arctic stratocumulus using ground-based lidar and cloud radar, J. Geophys. Res. Atmos., 114, https://doi.org/10.1029/2008JD011198, 2009.

van Diedenhoven, B., Cairns, B., Geogdzhayev, I. V., Fridlind, A. M., Ackerman, A. S., Yang, P., and Baum, B. A.: Remote sensing of ice crystal asymmetry parameter using multi-directional polarization measurements – Part 1: Methodology and evaluation with simulated measurements, Atmos. Meas. Tech., 5, 2361–2374, https://doi.org/10.5194/amt-5-2361-2012, 2012.

Wang, Y., Yang, P., Hioki, S., King, M. D., Baum, B. A., Di Girolamo, L., and Fu, D.: Ice cloud optical thickness, effective radius, and ice water path inferred from fused MISR and MODIS measurements based on a pixel-level optimal ice particle roughness model, J. Geophys. Res. Atmos., 124, 12 126–12 140, https://doi.org/10.1029/2019JD030457, 2019.

Wendisch, M., Pilewskie, P., Pommier, J., Howard, S., Yang, P., Heymsfield, A. J., Schmitt, C. G., Baumgardner, D., and Mayer, B.: Impact of cirrus crystal shape on solar spectral irradiance: A case study for subtropical cirrus, J. Geophys. Res. Atmos., 110, https://doi.org/10.1029/2004JD005294, 2005.

Wendisch, M., Yang, P., and Pilewskie, P.: Effects of ice crystal habit on thermal infrared radiative properties and forcing of cirrus, J. Geophys. Res. Atmos., 112, D08 201, https://doi.org/10.1029/2006JD007899, 2007.

Wilber, A. C.: Surface emissivity maps for use in satellite retrievals of longwave radiation, NASA, https://ntrs.nasa.gov/citations/19990100634, last access: 16 January 2023, 1999.

Wolf, K., Bellouin, N., and Boucher, O.: Simulated top-of-atmosphere (120 km) downward and upward solar and thermal-infrared irradiances and ice cloud optical thickness; calculated solar, TIR and net cloud radiative effect. Simulated with ice crystal properties for aggregates, droxtals, and plates based on Yang (2013)., https://doi.org/10.5281/zenodo.8159286, 2023.

Wylie, D. P. and Menzel, W. P.: Eight years of high cloud statistics using HIRS, J. Climate, 12, 170–184, https://doi.org/10.1175/1520-0442(1999)012<0170:EYOHCS>2.0.CO;2, 1999.

Yang, P. and Fu, Q.: Dependence of ice crystal optical properties on particle aspect ratio, J. Quant. Spectrosc. Radiat. Transfer, 110, 1604–1614, https://doi.org/10.1016/j.jqsrt.2009.03.004, 2009.

Yang, P., Liou, K. N., Wyser, K., and Mitchell, D.: Parameterization of the scattering and absorption properties of individual ice crystals, J. Geophys. Res. Atmos., 105, 4699–4718, https://doi.org/10.1029/1999JD900755, 2000.

Yang, P., Wei, H., Huang, H.-L., Baum, B. A., Hu, Y. X., Kattawar, G. W., Mishchenko, M. I., and Fu, Q.: Scattering and absorption property database for nonspherical ice particles in the near- through far-infrared spectral region, Appl. Opt., 44, 5512–5523, https://doi.org/10.1364/AO.44.005512, 2005.

Yang, P., Hong, G., Dessler, A. E., Ou, S. S. C., Liou, K.-N., Minnis, P., and Harshvardhan: Contrails and induced cirrus: optics and radiation, Bull. Am. Meteorol. Soc., 91, 473–478, https://doi.org/10.1175/2009BAMS2837.1, 2010.

Yang, P., Bi, L., Baum, B. A., Liou, K.-N., Kattawar, G. W., Mishchenko, M. I., and Cole, B.: Spectrally consistent scattering, absorption, and polarization properties of atmospheric ice crystals at wavelengths from 0.2 to 100 μm, J. Atmos. Sci., 70, 330–347, https://doi.org/10.1175/JAS-D-12-039.1, 2013.

Zhang, Y., Laube, M., and Raschke, E.: Numerical simulations of cirrus properties, Contrib. Atmos. Phys., 67, 109–120, 1994.

Zhang, Y., Macke, A., and Albers, F.: Effect of crystal size spectrum and crystal shape on stratiform cirrus radiative forcing, Atmos. Res., 52, 59–75, https://doi.org/10.1016/S0169-8095(99)00026-5, 1999.